

Joint inversions of ground deformation, extrusion flux and gas emissions using physics-based models for the Mount St. Helens 2004-2008 eruption

Ying Qi Wong¹ and Paul Segall¹

¹Stanford University

November 23, 2022

Abstract

With the increasing quantity and quality of data collected at volcanoes, there is growing potential to incorporate all the data into analyses of the magmatic system. Physics-based models provide a natural and meaningful way to bring together real-time monitoring data and laboratory analyses of eruption products, at the same time improving our understanding of volcanic processes. We develop a framework for joint inversions of diverse time series data using the physics-based model for dome-forming eruptions from \citeA{Wong2019}. Applying this method to the 2004-2008 eruption at Mount St. Helens, we estimate essential system parameters including chamber geometry, pressure, volatile content and material properties, from extruded volume, ground deformation and carbon dioxide emissions time series. The model parameter space is first sampled using the neighborhood search algorithm, then the resulting ensemble of models is resampled to generate posterior probability density functions on the parameters (missing citation); (missing citation). We find models that fit all three datasets well. Posterior PDFs suggest an elongate chamber with aspect ratio less than 0.55, located at \$9.0\$-\$17.2\$ km depth. Since the model calculates pressure change during the eruption, we can constrain chamber volume to \$64\$-\$256\$ km\$^3\$. Volume loss in the chamber is \$20\$-\$66\$ million m\$^3\$. At the top of the chamber, total (dissolved and exsolved) water contents are \$4.99\$-\$6.44\$ wt\% and total carbon dioxide contents are \$1560\$-\$3891\$ ppm, giving a porosity of 5.3-16.6\% depending on the conduit length. Compared to previous inversions using a steady-state conduit model, we obtain a lower magma permeability scale, radius and friction coefficient.

References

1 **Joint inversions of ground deformation, extrusion flux
2 and gas emissions using physics-based models for the
3 Mount St. Helens 2004-2008 eruption**

4 Ying-Qi Wong¹, and Paul Segall¹

5 ¹Department of Geophysics, Stanford University, Stanford, CA, USA

6 **Key Points:**

- 7 • Best-fit model produces satisfactory fits to all three datasets
8 • Elongate chambers of volume 64–256 km³ with centroid at 9.0–17.2 km depth
9 are preferred.
10 • Magma permeability, radius and friction are lower than estimates from inversions
11 with the steady-state model.

12 **Abstract**

13 With the increasing quantity and quality of data collected at volcanoes, there is growing
 14 potential to incorporate all the data into analyses of the magmatic system. Physics-
 15 based models provide a natural and meaningful way to bring together real-time mon-
 16 itoring data and laboratory analyses of eruption products, at the same time improving
 17 our understanding of volcanic processes. We develop a framework for joint inversions of
 18 diverse time series data using the physics-based model for dome-forming eruptions from
 19 Wong and Segall (2019). Applying this method to the 2004–2008 eruption at Mount St.
 20 Helens, we estimate essential system parameters including chamber geometry, pressure,
 21 volatile content and material properties, from extruded volume, ground deformation and
 22 carbon dioxide emissions time series. The model parameter space is first sampled using
 23 the neighborhood search algorithm, then the resulting ensemble of models is resampled
 24 to generate posterior probability density functions on the parameters (Sambridge, 1999b,
 25 1999a). We find models that fit all three datasets well. Posterior PDFs suggest an elon-
 26 gate chamber with aspect ratio less than 0.55, located at 9.0–17.2 km depth. Since the
 27 model calculates pressure change during the eruption, we can constrain chamber volume
 28 to 64 – 256 km³. Volume loss in the chamber is 20 – 66 million m³. At the top of the
 29 chamber, total (dissolved and exsolved) water contents are 4.99 – 6.44 wt% and total
 30 carbon dioxide contents are 1560 – 3891 ppm, giving a porosity of 5.3–16.6% depend-
 31 ing on the conduit length. Compared to previous inversions using a steady-state conduit
 32 model, we obtain a lower magma permeability scale, radius and friction coefficient.

33 **Plain Language Summary**

34 Data collected from volcanoes sheds light on the structure of the subsurface stor-
 35 age chamber and the migration of magma, thereby enhancing our understanding of vol-
 36 canic hazards. Integrating multiple datasets into analyses of a single eruption can resolve
 37 more details of the volcanic system. A theoretical model that predicts these data given
 38 some input parameters is needed to connect diverse volcanological datasets. We have pre-
 39 viously constructed a physics-based model that simulates the ascent of magma from the
 40 storage chamber to the surface through a pipe. The model is specialized for lava dome
 41 eruptions, such as the 2004–2008 at Mount St. Helens eruption, by taking into account
 42 magma solidification, gases coming out of solution and gases escaping from the system.
 43 The model is then used to calculate the lava dome volume, deformation of the land sur-
 44 face (detected by GPS) and rate of gas emissions. The model has several unknown pa-
 45 rameters. We run many iterations of the model with different combinations of param-
 46 eters and find models that fit all three datasets. This approach can constrain chamber
 47 geometry, pressure, gas content and material properties. Insights into this variety of sys-
 48 tem parameters would not have been possible with standard discipline-specific model-
 49 ing.

50 **1 Introduction**

51 In the past few decades, the expansion of both ground and satellite-based moni-
 52 toring systems, as well as advances in laboratory techniques to study volcanic products,
 53 have increased the quantity and quality of volcanological data. Since these observations
 54 are produced by common physical processes, physics-based models can provide a nat-
 55 ural and meaningful way to bring together these diverse data, at the same time improv-
 56 ing our understanding of volcanic processes.

57 A subset of models examines the last stages of magma's ascent through a volcanic
 58 conduit to the surface. These conduit flow models use fundamental conservation laws
 59 and rheologic models to simulate magma flow from chamber to surface. Phase changes
 60 affect magma properties such as density and viscosity which in turn regulate magma flux
 61 (e.g. Gonnermann & Manga, 2007). Models with varying levels of complexity have been

62 developed to investigate the processes controlling effusive and explosive behavior, as well
 63 as to study both steady-state and time-varying conduit flow (e.g. Jaupart & Allègre, 1991;
 64 Denlinger & Hoblitt, 1999; Papale, 2001; Mastin, 2002; De' Michieli Vitturi et al., 2013).
 65 These studies have elucidated critical processes that determine eruption style and du-
 66 ration, such as the complex feedbacks between magma velocity and crystallization ki-
 67 netics or gas escape that may produce cyclic lava discharge (Melnik & Sparks, 2005; Ko-
 68 zono & Koyaguchi, 2012). Connections to observations mainly involve qualitative com-
 69 parisons between observed and predicted magma flux, which is a direct model output.
 70 A few studies have gone further to couple conduit models to the surrounding crust to
 71 compare with observed ground deformation (e.g. Albino et al., 2011; Anderson & Segall,
 72 2011; Kawaguchi & Nishimura, 2015; Neuberg et al., 2018).

73 Prior work by Anderson and Segall (2013) demonstrated the utility of physics-based
 74 volcanic models in joint inversions of geophysical datasets. Their study focused on erup-
 75 tions that produce a lava dome at the surface. The 1D model simulates ascent of a three-
 76 phase magma, taking into account gas solubility and its effect on viscosity. Ascending
 77 magma causes the pressure in the chamber to drop, decreasing flow velocity exponen-
 78 tially in time. Model outputs were compared with extruded volume and geodetic data
 79 from the 2004-2008 eruption at Mount St. Helens using the Markov Chain Monte Carlo
 80 (MCMC) algorithm. Since conduit models can be highly non-linear, this probabilistic
 81 approach captures the range of model parameters consistent with the observations. Com-
 82 pared with traditional geodetic inversions, incorporating the physics-based model with
 83 extruded volume data allowed more parameters to be constrained, including initial cham-
 84 ber pressure, dissolved volatile content, and magma and chamber compressibility. The
 85 physics-based model is the crucial link that ties these datasets together.

86 In order to harness the full power of joint inversions using physics-based models,
 87 we need to capture the essential physical processes in the magmatic system. For dome-
 88 forming eruptions, slow ascent allows magma to crystallize gradually, an effect greatly
 89 simplified in the model of Anderson and Segall (2013). Gases exsolving during ascent
 90 may escape from the magma, which, together with crystallization, is critical to forming
 91 dense, degassed plugs in the shallow reaches of conduits (e.g. Kozono & Koyaguchi, 2012;
 92 Schneider et al., 2012). Wong et al. (2017) developed a steady-state physics-based model
 93 which incorporated crystallization and gas escape to study the quasi-steady phase of the
 94 2004-2008 Mount St. Helens eruption, when magma flux was approximately constant.
 95 Diverse data, including magma flux, dome rock porosity, solidus depth and plug depth,
 96 were used to derive distributions on critical system parameters. Wong and Segall (2019)
 97 extended this conduit model to study the temporal evolution of conduit flow. Scaling
 98 analysis showed that when chamber pressure declines slowly relative to the magma as-
 99 cent rate such as in dome-forming eruptions, steady-state solutions are inadequate in mod-
 100 eling the initial decline in magma flux, therefore requiring time-dependent solutions. Qual-
 101 itative comparisons with extruded volume, ground deformation and gas emissions time
 102 series identified the most influential system parameters.

103 In this study, we develop a framework for quantitative joint inversions of diverse
 104 time series datasets using the time-dependent conduit flow model from Wong and Segall
 105 (2019). Given extrusion volume, ground deformation and carbon dioxide emissions time
 106 series from the 2004-2008 Mount St. Helens eruption, we estimate essential system prop-
 107 erties including chamber geometry, initial pressure, volatile content and material prop-
 108 erties. A suitable inversion technique for physics-based models should account for the
 109 non-linearity of volcanic systems, therefore we prefer probabilistic methods that estimate
 110 not only an optimal solution but also the range of admissible solutions (? , ?). At the same
 111 time, since the model is computationally expensive, we are unable to use simple stochas-
 112 tic methods such as MCMC that require millions of forward model evaluations. Based
 113 on these considerations, we choose to apply the Neighborhood Algorithm which is triv-

114 ially parallelizable and can build probability density functions (PDFs) of the relevant
 115 system parameters (Sambridge, 1999b, 1999a).

116 **2 Methods**

117 **2.1 Physics-based model for Mount St. Helens plumbing system**

118 We have developed a physics-based model of the plumbing system at Mount St.
 119 Helens to simulate magma ascent from an ellipsoidal magma chamber through a conduit
 120 to the surface (Figure 1). The model is one-dimensional (radially-averaged). Properties
 121 in the chamber are taken as lumped parameters evolving with time, while properties in
 122 the conduit are modeled in both time and depth. In this section, we present a brief overview
 123 of the chamber-conduit model; details can be found in Wong and Segall (2019).

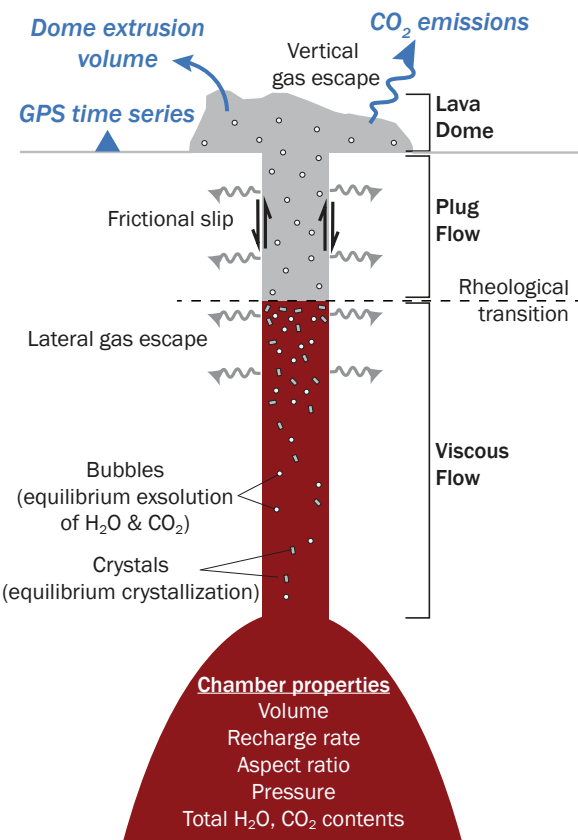


Figure 1. Model setup, adapted from Wong and Segall (2019). Magma ascends viscously from a chamber through a cylindrical conduit, where it undergoes crystallization, gas exsolution and gas escape, eventually transitioning to a solid plug that slides along the conduit walls. The three datasets used to constrain model parameters are shown in blue.

124 At the beginning of the eruption, pressure in the chamber exceeds the magma col-
 125 umn weight and drives flow out of the chamber towards the surface. The ascending magma
 126 exsolves volatiles and crystallizes. Once enough volatiles exsolve, the gas volume frac-
 127 tion exceeds the percolation threshold and permits gases to escape from the system both
 128 vertically through the conduit and laterally through the conduit walls. The combined
 129 effects of gas exsolution, gas escape and crystallization strongly influence viscosity and
 130 cause the magma flow regime to evolve naturally from viscous flow at depth to solid plug

sliding in the shallow part of the conduit. Removal of magma from the chamber lowers the chamber volume and pressure over time, which decreases the magma ascent velocity asymptotically towards zero.

2.1.1 Conduit flow model

Magma consists of solids, liquid melt which contains dissolved water (H_2O) and carbon dioxide (CO_2), as well as exsolved volatiles, giving its density ρ as

$$\rho = \rho_s \phi_s + \rho_l \phi_l c_1 + \rho_g \phi_g \quad (1)$$

For each phase, the density and volume fraction are ρ and ϕ respectively. Subscripts indicate the phase: s for solids, l for liquid melt, and g for gases. The term c_1 accounts for dissolved volatiles and depends on the dissolved mass concentrations of H_2O and CO_2 (χ_h^d, χ_c^d), which are modeled as functions of pressure and temperature using the solubility relations from Liu et al. (2005). We derive the solid volume fraction ϕ_s by assuming isothermal equilibrium crystallization of the water-saturated Mount St. Helens dacite (Pallister et al., 2008; Schneider et al., 2012).

These component phases affect magma viscosity η , which is a combination of the melt viscosity η_m and the relative viscosity increase due to solids η_s ,

$$\eta = \eta_m(\chi_h^d, \chi_c^d, T) \eta_s(\phi_s, \dot{\gamma}), \quad (2)$$

We apply the dacite melt viscosity model of Whittington et al. (2009), which depends on dissolved volatile content and temperature T . For the relative viscosity increase due to solids, we apply the model of Costa (2005) and Caricchi et al. (2007) which incorporates a dependence on strain rate $\dot{\gamma}$. The effect of bubbles on viscosity is neglected since porosity of the 2005 Mount St. Helens dome lavas is relatively low, thus the effect of crystals predominates (Llewellyn & Manga, 2005).

Applying these magma properties, the governing equations for 1D conduit flow are

$$v = v_{\text{visc}} + v_{\text{fric}} = \frac{\tau_R R}{4\eta} + 2v_r \exp\left(-\frac{f_0}{a}\right) \sinh\left(\frac{\tau_R}{a\sigma_c}\right), \quad \text{where } \tau_R = -\frac{R}{2} \left(\frac{\partial p}{\partial z} + \rho g \right) \quad (3)$$

$$\frac{\partial}{\partial t}(\rho_s \phi_s + \rho_l \phi_l) = -\frac{\partial}{\partial z}[(\rho_s \phi_s + \rho_l \phi_l)v] \quad (4)$$

$$\frac{\partial}{\partial t} \left(\chi_h^d \rho_l \phi_l c_1 + \frac{1}{1+\Gamma} \rho_g \phi_g \right) = -\frac{\partial}{\partial z} \left[\left(\chi_h^d \rho_l \phi_l c_1 + \frac{1}{1+\Gamma} \rho_g \phi_g \right) v + \frac{1}{1+\Gamma} \rho_g \phi_g (v_g - v) \right] - \frac{2\rho_g \phi_g u_g}{R(1+\Gamma)} \quad (5)$$

$$\frac{\partial}{\partial t} \left(\chi_c^d \rho_l \phi_l c_1 + \frac{\Gamma}{1+\Gamma} \rho_g \phi_g \right) = -\frac{\partial}{\partial z} \left[\left(\chi_c^d \rho_l \phi_l c_1 + \frac{\Gamma}{1+\Gamma} \rho_g \phi_g \right) v + \frac{\Gamma}{1+\Gamma} \rho_g \phi_g (v_g - v) \right] - \frac{2\Gamma \rho_g \phi_g u_g}{R(1+\Gamma)} \quad (6)$$

The radially-averaged momentum balance (equation 3) gives magma velocity v as a combination of incompressible, steady, laminar Poiseuille Flow v_{visc} and a rate-dependent frictional slip boundary condition v_{fric} (Rice et al., 2001) (full derivation in Wong and Segall (2019)). Flow is driven by the difference between the vertical pressure gradient $\partial p / \partial z$ and the gravitational load ρg , giving shear stress τ_R . The conduit has constant radius R . The conduit walls have depth-dependent effective normal stress $\sigma_c(z)$, which is the difference between lithostatic normal stress and hydrostatic pore pressure, $(\rho_{\text{lith}} - \rho_{\text{hyd}})gz$, neglecting tectonic and topographic contributions. Wall friction is parameterized by the nominal coefficient f_0 , rate-dependence a , and reference velocity v_r . Deep in the conduit, where η is low and σ_c is high, v_{visc} predominates and magma flows viscously. In the shallower conduit, magma solidification increases η while σ_c decreases, increasing v_{fric} until frictional sliding becomes the dominant flow regime.

Continuity for solids and liquids (equation 4) reflects the exchange of mass as liquid melt solidifies during ascent. Continuity for H_2O (equation 5) contains both dissolved and exsolved components. Transient mass changes are balanced by the flux of volatiles as well as vertical and lateral gas flow out of the conduit at gas velocities v_g and u_g respectively (e.g. Kozono & Koyaguchi, 2012; Schneider et al., 2012). The term $\Gamma = (1 -$

170 $m_h)\mathcal{M}_c/(m_h\mathcal{M}_h)$ is the mass ratio of exsolved CO₂ to H₂O, where m_h is the mole fraction
 171 of water in the vapor phase and $\mathcal{M}_c, \mathcal{M}_h$ are the molar masses of CO₂ and H₂O respectively.
 172 A similar form describes the continuity of CO₂ (equation 6).

173 To model gas escape from the system, we apply Darcy's Law while assuming chemical
 174 and mechanical equilibrium between the gas phase and the ambient melt (Jaupart
 175 & Allègre, 1991; Schneider et al., 2012; Kozono & Koyaguchi, 2012). This implies that
 176 gas and melt pressures are the same. The gas velocities are given by

$$(v_g - v) = \frac{k_{\text{mag}}}{\eta_g} \frac{\partial p}{\partial z} \quad (7)$$

$$u_g = \frac{k_{\text{lat}}}{\eta_g} \frac{p - p_{\text{hyd}}}{2R}, \quad (8)$$

177 where η_g is the gas viscosity, and $p_{\text{hyd}} = \rho_{\text{hyd}} g z$ is the hydrostatic pressure. In vertical
 178 gas escape, gas flows through the magma only, thus the permeability constant in equation
 179 7 is the magma permeability k_{mag} modeled using the Carman-Kozeny relation,

$$k_{\text{mag}} = k_c \phi_g^3, \phi_g > \phi_{gc}, \quad (9)$$

180 where k_c is a scaling constant, ϕ_g is the gas volume fraction (porosity) and ϕ_{gc} is the per-
 181 colation threshold, which is the minimum porosity to form interconnected pathways and
 182 has a typical value of $\sim 30\%$ (Klug & Cashman, 1996; Saar & Manga, 1999; Blower, 2001).
 183 In lateral gas escape, gas flows through both magma and the wall rock. The lateral per-
 184 meability k_{lat} is a harmonic average of k_{mag} and the crustal permeability model from Manning
 185 and Ingebritsen (1999).

186 2.1.2 Boundary and initial conditions

187 Taking into account the constitutive relations, the model solves for four field vari-
 188 ables at each depth and time: pressure, velocity, gas volume fraction (porosity) and mole
 189 fraction of water in the vapor phase, compiled into the vector $y(z, t) = [p, v, \phi_g, m_h](z, t)$.
 190 The governing equations provide $4(N_z - 1)$ equations, where N_z is the number of depth
 191 points. This system of equations requires 4 boundary conditions to be complete: pres-
 192 sure and volatile contents in the chamber, and pressure at the top of the conduit.

193 At the beginning of the eruption, chamber pressure is greater than the magma col-
 194 umn weight to drive flow. As the eruption proceeds, magma outflux causes the cham-
 195 ber pressure to decrease, while influx from a deeper source may increase the chamber
 196 pressure (e.g. Segall, 2013),

$$\frac{dp_{\text{ch}}}{dt} = \frac{q_{\text{in}} - q_{\text{out}}}{\rho_0 V_0 (\beta_{\text{mag}} + \beta_{\text{ch}})} = \frac{\Omega(p_{\text{deep}} - p_{\text{ch}}) - \pi R^2 v_{\text{ch}}}{V_0 (\beta_{\text{mag}} + \beta_{\text{ch}})}, \quad (10)$$

197 where Ω is a proportionality constant linking recharge in the chamber to the magmatic
 198 static head between the chamber and a deep reservoir at pressure p_{deep} , v_{ch} is the velocity at
 199 the conduit base, V_0 is the initial chamber volume, while β_{mag} and β_{ch} are the magma
 200 and chamber compressibilities respectively,

$$\beta_{\text{mag}} = \frac{1}{\rho} \frac{\partial \rho}{\partial p}, \quad \beta_{\text{ch}} = \frac{1}{V} \frac{\partial V}{\partial p}, \quad (11)$$

201 where ρ, p are evaluated at the center of the chamber (Anderson & Segall, 2011). Magma
 202 density in the chamber is calculated using equation 1, while chamber center pressure is
 203 the sum of pressure at the conduit inlet and magmatic head from the chamber top
 204 to center. Chamber compressibility is estimated from the numerical results for different
 205 ellipsoidal chamber shapes (Amoruso & Crescentini, 2009). Scaling analysis of equation
 206 10 with equations 4–6 shows that if the ascent timescale is much shorter than the cham-
 207 ber pressure evolution, the time-dependent model should approximate steady-state so-
 208 lutions evaluated at the identical chamber pressure (Wong & Segall, 2019). This could

209 occur if the chamber volume is large ($> 1000 \text{ km}^3$). On the other hand, if the ascent
 210 and chamber pressure evolution timescales are comparable, full time-dependent solutions
 211 are needed to model conduit flow.

212 Other boundary conditions are the H_2O and CO_2 mass concentrations in the cham-
 213 ber χ_h^{ch}, χ_c^{ch} . Using the solubility equations, the volatiles are separated into dissolved and
 214 exsolved components to determine the gas volume fraction and mole fraction of water
 215 to carbon dioxide at the base of the conduit. Finally, the pressure at the conduit exit
 216 is assumed to be atmospheric pressure.

217 We initialize the model with the steady-state solution given specified boundary con-
 218 ditions at $t = 0$ using the code from Wong et al. (2017). Natural eruptions clearly do
 219 not start from steady-state, and future work is needed to derive more realistic eruption
 220 onsets that simulate acceleration of partially solidified conduit magma leftover from lava
 221 dome eruptions in the 1980s.

222 2.1.3 Model parameters and prior bounds

223 To solve each forward model, we specify magma chamber properties (aspect ratio,
 224 volume), conduit geometry (length, radius), material properties (magma permeability
 225 scale, conduit wall friction), and conduit base boundary conditions (initial pressure, volatile
 226 contents). In this study, we set the recharge rate Ω to zero because the extruded volume
 227 time series appears to flatten out at the end of the eruption, suggesting that there is no
 228 recharge. Previous inversions also suggest that syn-eruptive recharge is minor (Anderson
 229 & Segall, 2013). Sensitivity analyses showed that the observations are insensitive to per-
 230 colation threshold, thus we fix it to the typical value of 30% (Wong & Segall, 2019). The
 231 chamber depth is uniquely determined from the chamber volume, aspect ratio and con-
 232 duit length. For a consistent description of the initial conduit base pressure for differ-
 233 ent conduit lengths, the total pressure at the conduit base p_{ch} is defined in terms of an
 234 excess pressure Δp_0 at $t = 0$,

$$235 p_{ch}(t=0) = p_{atm} + \rho_l g L + \Delta p_0, \quad (12)$$

236 where p_{atm} is the pressure at the top of the conduit and ρ_l is the melt phase density. We
 237 choose a wide range for the model parameter prior bounds to minimize the influence of
 prior assumptions on the posterior probabilities (Table 1).

238 2.2 Data from the 2004-2008 Mount St. Helens eruption

239 The 2004-2008 Mount St. Helens eruption began with swarms of shallow volcano-
 240 tectonic earthquakes on September 23, 2004 that culminated in a series of explosions start-
 241 ing on October 1, 2004 (Moran et al., 2008; Scott et al., 2008). These explosions gave
 242 way to lava extrusion under the crater glacier, forming a large welt on the south side of
 243 the 1980s lava domes (Vallance et al., 2008; Scott et al., 2008; Dzurisin et al., 2015). The
 244 new lava eventually broke through the glacier and was first seen on October 11, 2004.
 245 Thereafter, a series of lava spines, some of which resembled “whalebacks”, were extruded
 246 on the crater floor. Extrusion was accompanied by tilt cycles (Vallance et al., 2008; An-
 247 derson et al., 2010) and repetitive low-frequency and hybrid “drumbeat” earthquakes
 248 that were suggested to be caused by stick-slip motion of a solid plug ascending through
 249 the conduit (Moran et al., 2008; Iverson, 2008). After 3.3 years, eruptive activity waned
 250 and finally ended in January 2008 (Dzurisin et al., 2015).

251 During the eruption, a wide variety of data was collected. Three time series datasets
 252 were chosen to compare with model predictions: (a) extruded volume which indicates
 253 the evolution of exit velocity, (b) gas emissions which inform us about volatile content
 254 and permeability, and (c) ground deformation which reflects pressure change and geom-
 255 etry of the magma reservoir. We also include constraints on the porosity of magma ex-
 256 iting the conduit.

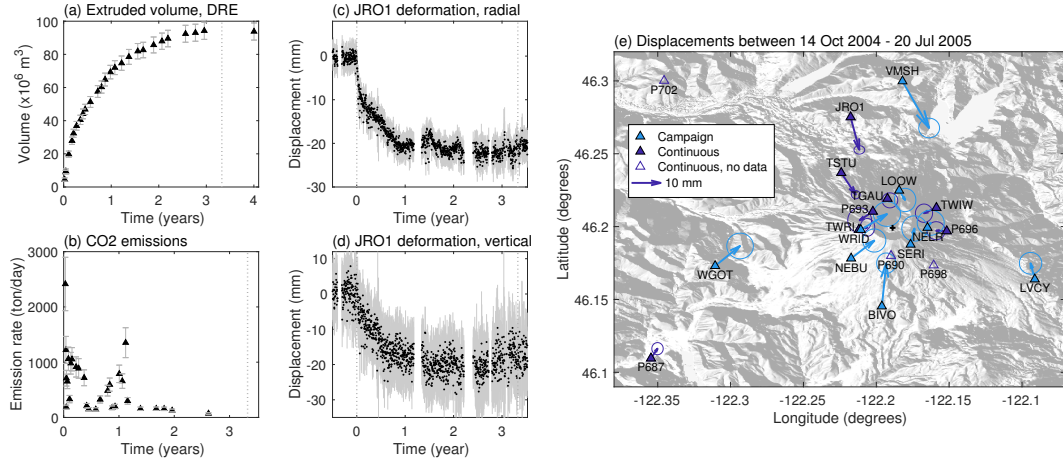


Figure 2. Datasets from the 2004–2008 Mount St. Helens eruption used in this study: (a) Dense rock equivalent (DRE) time series of extruded volume. (b) Carbon dioxide emission rates. (c-d) Radial and vertical deformation at 14 continuous GPS stations were used, here showing, as an example, JRO1, the only nearby station in operation at the eruption onset. (e) Map view of stations within 20 km of the volcano with displacement vectors between two campaigns during the eruption (14 October 2004 – 20 July 2005). Another 2 stations (KELS and P421) are outside this map view. Light blue filled triangles are campaign stations, dark blue filled triangles are continuous stations in operation during this period, and dark blue open triangles are continuous stations that started operation after 14 October 2004. Black cross denotes the center of the crater.

257

2.2.1 Extruded volume

258
259
260
261
262
263
264
265
266
267
268

Differential Digital Elevation Models (DEMs) using aerial photogrammetry tracked the growth of the lava dome in the crater (Schilling et al., 2008; Dzurisin et al., 2015) (Figure 2a). In the initial few weeks of the eruption, lava was extruded beneath the crater glacier, precluding direct observation of dome growth. Deformation of the glacier surface showed a welt of approximately 10 ± 1 million m^3 by October 11, 2004. After that, lava broke the surface of the glacier and direct observations of the lava dome growth became possible to generate the widely-used time series of dome volume change. The total extruded volume reached a maximum of 94.2 million m^3 , while uncertainties in these volume estimates are $\sim 4\%$. Post-eruption volume decline is attributed to dome compaction. From this data, we remove an estimated dome porosity of 10% to obtain the dense rock equivalent (DRE) volume (Cashman et al., 2008; Smith et al., 2011).

269
270
271

From the model predictions, we calculate the DRE extruded volume from the extrusion rate by excluding the gas volume fraction and integrating over time (Anderson & Segall, 2011),

$$V_{\text{ex}}(t) = \pi R^2 \int_0^t v(z=0, t)[1 - \phi_g(z=0, t)] dt, \quad (13)$$

272
273
274
275
276

We compare the predicted and observed extruded volume time series to assess model fit. We additionally impose a constraint that the increase in extruded volume over the final two measurements, recorded at 3.0 and 4.0 years after the eruption start, is small (i.e. less than $4 \times 10^6 \text{ m}^3$, the average error in the extruded volume measurements) to ensure that the final extrusion flux is approximately zero.

277 ***2.2.2 Carbon dioxide emissions***

278 During the eruption, emissions of carbon dioxide generally decayed with time. These
 279 data, along with measurements of sulfur dioxide and hydrogen sulfide, were collected via
 280 aircraft sampling of the vapor plume (Gerlach et al., 2008) (Figure 2b). Gases escaping
 281 both vertically through the conduit and laterally through the wall rocks may be observed
 282 at the surface. However, in calculating the gas flux at the surface, we approximate that
 283 all CO₂ in the plug escaped vertically. Laboratory measurements of permeability indi-
 284 cate that vertical permeability is much higher than lateral permeability (Gaunt et al.,
 285 2014). In addition, we would expect a time lag in gas emissions if lateral gas percola-
 286 tion was important. This delay was not observed: emissions decayed below the detec-
 287 tion threshold before the end of the eruption. Model predictions thus serve as an upper
 288 bound on vertical gas escape. We calculate the carbon dioxide emissions as

$$Q_c^{ex}(t) = \pi R^2 \frac{\Gamma}{1 + \Gamma} \rho_g \phi_g (v_g - v) \Big|_{z=0}, \quad (14)$$

289 where all variables are evaluated at the surface. Note that there is also flux of gas trans-
 290 ported within pores in the magma, however, this contribution is small since v is much
 291 smaller than ($v_g - v$) at the surface.

292 ***2.2.3 Ground deformation from GPS stations***

293 The eruption was monitored by a network of continuous and campaign Global Po-
 294 sitioning System (GPS) stations around the volcano (Figure 2c-e). Most of these sta-
 295 tions were installed after the eruption began. Only one station, JRO1 at the Johnston
 296 Ridge Observatory, captured the eruption onset, which was characterized by rapid de-
 297 flationary motion of about 10 mm in two weeks (Lisowski et al., 2008; Anderson & Segall,
 298 2013).

299 To obtain the volcanic deformation signal, we downloaded and processed position
 300 time series from continuous GPS stations in the USGS Pacific Northwest Network, fo-
 301 cusing on stations within 100 km of Mount St. Helens. Stations on Mount Rainier were
 302 omitted due to strong measurement drift due to snow. The region around Mount St. He-
 303 lens experiences long-term deformation due to convergence of the North American and
 304 Juan de Fuca plates, slow slip events, seasonal fluctuations and volcano-related defor-
 305 mation. We first identify slow slip time intervals between 1999 and 2020 using the rel-
 306 ative strength index (Crowell et al., 2016) on 36 stations located between 20 and 100 km
 307 of the volcano. A slow slip event must be identified by at least two stations in order to
 308 be accepted. Next, we simultaneously estimated tectonic deformation rates, slow slip off-
 309 sets, sinusoidal seasonal effects and amplitudes for power law noise including white, flicker
 310 and random walk using the Maximum Likelihood Estimation (MLE) approach (Mao et
 311 al., 1999; Langbein, 2004; Williams, 2008) on the post-eruption position time series (2012–
 312 2020) which has no discernible volcanic deformation. We assume that tectonic deforma-
 313 tion, seasonal variability and noise amplitudes are the same before and after 2012. We
 314 remove the tectonic deformation and seasonal signal from the whole time series, and ap-
 315 ply the noise amplitudes to the covariance matrix of syn-eruptive measurements. Off-
 316 sets due to slow slip events and antenna maintenance before 2012 were removed by tak-
 317 ing averages before and after the offset. The result is the deformation due to volcanic
 318 activity.

319 Of the GPS stations within 100 km of Mount St. Helens, 21 are within 60 km of
 320 the volcano and recorded displacements during the eruption period. 8 of these 21 con-
 321 tinuous stations only recorded the latter half of the eruption when deformation was lim-
 322 ited and thus were excluded from the inversions. For the remaining 13 stations, the co-
 323 variance matrix for the deformation time series was modeled using amplitudes obtained
 324 in the MLE and uncertainties in the tectonic velocity and SSE offset estimates. Note that

325 data during slow slip events were removed from the data, causing gaps in the time se-
326 ries, because we do not model the time-dependent deformation caused by these events.

327 Additional campaign GPS measurements from 9 stations between October 14, 2004
328 and July 20, 2005 were incorporated. This time period spans 0.05 to 0.8 years after erup-
329 tion onset. Based on the continuous station data, this period encapsulates a large pro-
330 portion of the total deformation. These campaign measurements can therefore provide
331 additional constraints on chamber geometry and depth. Tectonic velocities at the con-
332 tinuous GPS stations were linearly interpolated (i.e. assuming constant plate strain and
333 rotation rate) to remove tectonic velocities at the campaign GPS stations. Slow slip off-
334 sets and seasonal fluctuations were ignored due to lack of constraints, which may bias
335 the campaign displacements. In particular, vertical deformation at nearby, high eleva-
336 tion stations had high errors.

337 From the model-predicted pressure decay time series, we calculate radial displace-
338 ments using the expressions of Yang et al. (1988) for prolate spheroidal chambers. We
339 do not consider the effect of conduit tractions on surface displacements, because the GPS
340 stations are far from the vent relative to the plug length.

341 *2.2.4 Additional constraint on magma porosity*

342 As an additional inversion constraint, we considered the porosity of dome lava spec-
343 imens collected by helicopter (Pallister et al., 2008; Thornber et al., 2008). These spec-
344 imens consist of dense, light-gray dacite with porosities below 10% and vesicular, dark
345 gray to red dacite with porosities of 25–40% (Cashman et al., 2008). One helium pyc-
346 nometer measurement indicated a connected porosity of 30.4% (Cashman et al., 2008).
347 Five intact samples with no deformation textures showed porosity declining from 19.7%
348 to 10.3% after two years (Smith et al., 2011). Applying the porosity time series from Smith
349 et al. (2011) directly to the inversion is challenging because of the small number of sam-
350 ples and the fact that they consist of intact, centimeter to meter scale samples which may
351 or may not be representative of the average porosity across the tens-of-meter scale con-
352 duct. Therefore we opt for a simple constraint that admits only models whose predicted
353 porosity time series is entirely less than the maximum observed porosity of 40%.

354 **2.3 Inversions using the neighborhood algorithm**

355 We apply the neighborhood algorithm (Sambridge, 1999b, 1999a) to estimate crit-
356 ical properties of the Mount St. Helens plumbing system. Previous studies have applied
357 this algorithm to volcano deformation to determine the location and volume change of
358 magma chambers, as well as to model dike geometry from InSAR data (e.g. Pritchard
359 & Simons, 2002; Fukushima et al., 2005). The neighborhood algorithm consists of two
360 stages: (1) the model space search and (2) the ensemble appraisal.

361 *2.3.1 Searching the model space*

362 Stage 1 generates an ensemble of models by searching the model space to find mod-
363 els that have high posterior probabilities (Sambridge, 1999b). This stage is akin to an
364 adaptive grid search. In this section, we first define the posterior probability and then
365 describe the search algorithm.

366 The posterior probability $p(\mathbf{m}|\mathbf{d})$ of each model is

$$p(\mathbf{m}|\mathbf{d}) \propto L(\mathbf{d}|\mathbf{m})p(\mathbf{m}) \quad (15)$$

367 where $L(\mathbf{d}|\mathbf{m})$ is the data likelihood and $p(\mathbf{m})$ is the prior probability distribution. In
368 this study, we assume uniform priors on the model parameters, however this inversion
369 scheme can be easily adjusted to incorporate other priors. Uniform priors have constant

370 $p(\mathbf{m})$ while \mathbf{m} is within pre-defined bounds. The posterior probability therefore depends
 371 only on the likelihood,

$$L(\mathbf{d}|\mathbf{m}) \propto \exp\left[-\frac{1}{2}\sum_k \frac{1}{w_k} \Phi\right], \quad (16)$$

$$\text{where } \Phi = \sum_k \left[w_k (\mathbf{d}_k - \hat{\mathbf{d}}_k)^T \Sigma_k^{-1} (\mathbf{d}_k - \hat{\mathbf{d}}_k) \right], \quad (17)$$

372 where k denotes the dataset (extruded volume, continuous GPS positions, campaign GPS
 373 displacements, CO₂ emissions) and Φ is the joint misfit to the data. For the k th dataset,
 374 w_k is the weight, \mathbf{d}_k are the observed data, $\hat{\mathbf{d}}_k$ are the predicted data, and Σ_k is the co-
 375 variance matrix.

376 The simplest joint misfit is obtained by assigning equal weights ($w_k = 1$) for all
 377 k datasets. However, initial tests show that this approach does not find well-fitting so-
 378 lutions to this problem because of the high scatter in the CO₂ emissions. This scatter
 379 arises from unmodeled processes (e.g. crack propagation in the plug that allows sudden
 380 release of gases) or measurement errors (e.g. wind dispersal of emissions) that cannot
 381 be captured by the current physics-based model, which can only predict smoothly de-
 382 caying solutions. Therefore we need to reduce the weight of the CO₂ emissions w_{CO_2} to
 383 prevent the misfit to the CO₂ emissions from dominating the total misfit. To determine
 384 w_{CO_2} , we bin the emissions into months and examine the variability among measurements
 385 in the same month (Figure 3). During the 2.6-year observation duration, eight months
 386 had more than one observation (months 0, 1, 2, 3, 5, 10, 11, 13). In these eight months,
 387 the root-mean-square deviation from the monthly average ranged from 12 – 597 ton/day.
 388 Normalizing the high estimate of 597 ton/day by the median measurement error of 97
 389 ton/day gives a scale factor of 6.15. Therefore we assign w_{CO_2} as the reciprocal of the
 390 square of this scale factor to get units of variance, giving $w_{\text{CO}_2} = 1/(6.15^2) = 0.0264$.
 391 Weights to all other datasets were assigned as 1.

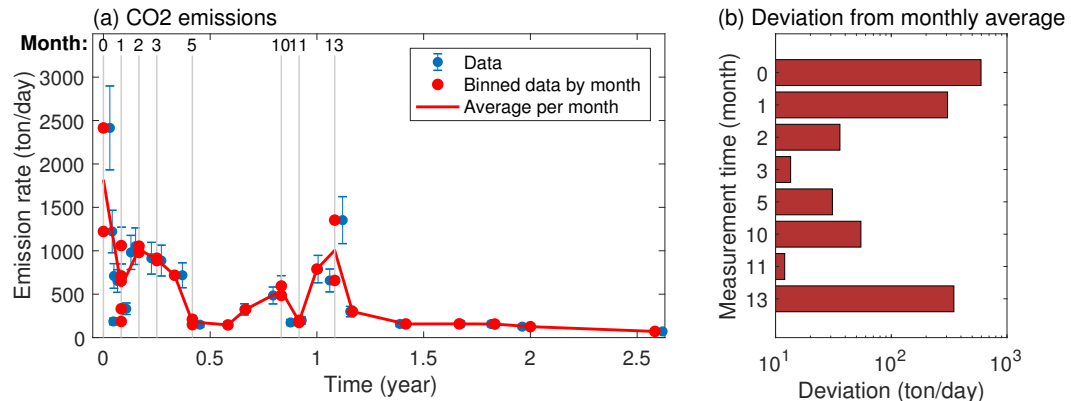


Figure 3. Determining the weight for the CO₂ emissions time series. (a) Observed emissions (blue dots with error bars) and binned by month (red dots). Red line tracks the average for each month. Months with more than one observation are indicated at the top of the axis. (b) Root-mean-square of deviations of observed CO₂ emissions from the monthly average for the 8 months that had multiple observations.

392 The search algorithm in the Stage I is as follows: first, N_s model parameter com-
 393 binations are randomly chosen to run the forward model and evaluate the joint misfit
 394 (equation 17). The forward model evaluations can be run in parallel. From this set of
 395 models, the best-fitting N_r models, where $N_r \leq N_s$, are selected for the next iteration.
 396 Since we use uniform priors, finding models that minimize the misfit is equivalent to max-

imizing the posterior probability. In the next iteration, a new set of N_s/N_r models is generated in the neighborhood of each selected model. As an example, if $N_s = 200$, $N_r = 100$, the 100 best-fitting models are chosen at this stage, and 2 new points are generated in the neighborhood of each of these 100 models to generate a total of 200 new points. The “neighborhood” is defined using Voronoi cells, where cell boundaries are the midpoint of two models. Sambridge (1999b) provides an efficient method to calculate these cell boundaries. The misfits of each of these new models are then evaluated, and the process of selecting well-fitting cells and generating new models and misfits is repeated until the minimum misfit approaches a constant.

The neighborhood search is simple to implement and only requires two tuning parameters N_s, N_r which influence the effectiveness of the model space search. Large N_s, N_r produce a more exploratory search; small N_s, N_r improve the algorithm’s capability as an optimizer although it may become susceptible to local minima.

2.3.2 Appraising the ensemble of models

Stage 2 resamples the ensemble of models using a Gibbs Sampler to generate probability density functions (PDFs) of the model parameters (Sambridge, 1999a). Within the neighborhood of each model, the posterior probability $p(\mathbf{m}|\mathbf{d})$ is assumed to be constant, so that no new forward model runs are required. Starting from a high probability model, the Gibbs Sampler takes a random step along each parameter axis in turn according to the conditional probability along the current axis $p(m_j|\mathbf{m}_{-j}, \mathbf{d})$ (the probability of parameter m_j given all other specified parameters \mathbf{m}_{-j}). Following Sambridge (1999a), we generate this random step using the rejection method: first, a uniform random deviate m_j^{prop} is generated within the specified model parameter bounds. The proposed step is then compared with the maximum probability along that axis and another uniform random deviate r on the interval (0,1). The proposed step is accepted if

$$\log r \leq \log p(m_j^{\text{prop}}|\mathbf{m}_{-j}, \mathbf{d}) - \log p(m_j^{\text{max}}|\mathbf{m}_{-j}, \mathbf{d}). \quad (18)$$

If m_j^{prop} is rejected, this procedure is repeated until a step is accepted. This procedure is repeated for each parameter axis, and then on subsequent samples. The rejection method only compares the log probabilities between two models and does not require calculation of the actual probabilities, thereby avoiding numerical underflow issues.

Two input parameters are needed for the Gibbs sampler: the length of each Gibbs sampling chain, and the number of chains. We test different values for these two parameters until the PDFs converge. In this study, a general rule is that the chain length should be at least 2000 and at least 50 chains should be sampled.

3 Results

3.1 The model parameter space

For Stage 1 of the neighborhood algorithm, we run the algorithm with $N_s = N_r = 200$ for 600 iterations, which was sufficient for model parameters to converge and for maximum model likelihoods to reach a stable value (Figure 4). Parameters for the maximum likelihood model lie well within the prescribed bounds. After 20 iterations, we reduced the lower bound of conduit radius from 20 m to 10 m as the best fit model appeared to be very close to 20 m. Chamber aspect ratio and volume appear to converge after about 400 iterations. Other parameters converge more slowly, eventually reaching a stable maximum likelihood model (red line, parameters in Table 1). During the search, the algorithm also explored a region distinct from the global maximum likelihood (pink line in Figure 4). On closer inspection, we observe that these models have non-smooth solutions caused by a slight numerical instability at the percolation threshold. Smoothing the percolation threshold transition removes this instability, but the predicted data for these

Table 1. Model parameters with their prior bounds, best-fit values from the neighborhood search, as well as the median model and 90% credible interval from the neighborhood appraisal.

Symbol	Description	Prior bounds	Best-fit from search	Median model	90% credible interval
<i>Chamber properties</i>					
α	Aspect ratio (width/height)	0.05 – 1	0.30	0.36	0.13 – 0.55
V_0	Volume (km^3)	10 – 500	130	136	64.1 – 256
Ω	Recharge rate ($\text{m}^3 \text{ day}^{-1} \text{ Pa}^{-1}$)	0 (fixed)			
<i>Conduit geometry</i>					
L	Length (km)	2 – 8	4.55	4.75	2.95 – 5.79
R	Radius (m)	10 – 100	20.6	22.1	11.9 – 35.8
<i>Material properties</i>					
k_c	Magma permeability scale (m^2)	$10^{-20} – 10^{-10}$	$10^{-13.5}$	$10^{-13.5}$	$10^{-14.7} – 10^{-12.1}$
ϕ_{gc}	Percolation threshold	0.2 – 0.4	0.25	0.25	0.21 – 0.28
f_0	Nominal coefficient of friction	0.01 – 0.8	$10^{-1.66}$	$10^{-1.66}$	$10^{-1.94} – 10^{-1.26}$
a	Rate-dependence of friction	$10^{-3} – 10^{-1}$	$10^{-2.69}$	$10^{-2.77}$	$10^{-2.97} – 10^{-2.37}$
<i>Conduit base boundary conditions</i>					
Δp_0	Excess pressure at $t = 0$ (MPa)	5 – 50	18.9	18.9	11.6 – 26.3
$\chi_{h^*}^{ch}$	Total water content (wt%)	3 – 7	5.55	5.73	4.99 – 6.44
χ_c^{ch}	Total carbon dioxide content (ppm)	100 – 5000	2925	2802	1560 – 3891

models produce poor fits to the observations. In particular, these solutions fail to satisfy the zero flux condition at the end of the eruption. Therefore we reject these non-smooth solutions as unphysical.

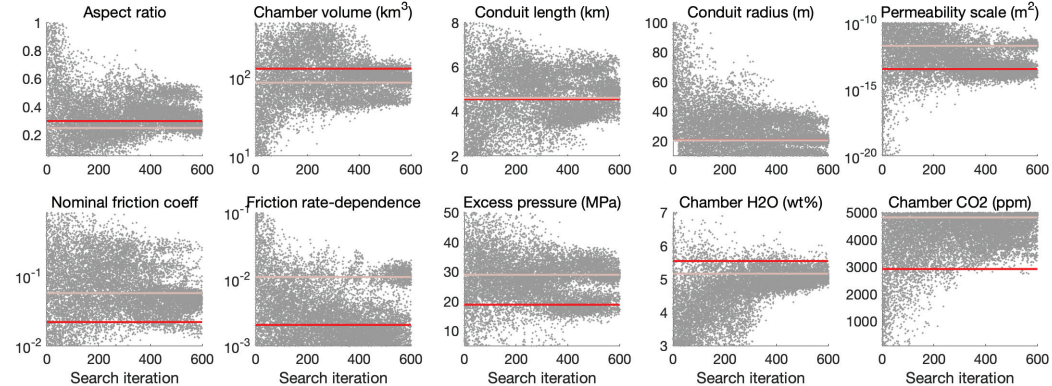


Figure 4. Model parameters at each neighborhood search iteration. Model parameter bounds are the limits of the vertical axis. Red line marks the best-fit model. Pink line marks one model with non-smooth solutions.

This ensemble of models produces reasonable fits to the combined dataset (Figure 5). Predicted extruded volume from the best-fit model to the combined dataset (red line) matches early observations well, but underpredicts the data at later times because of the higher measurement error. Similarly, the models accepted in the appraisal step (pink envelope) closely follow early volume estimates but show a wider range of final extruded volume. The predicted JRO1 radial displacement follows the observations well. Due to the lower weight applied to the CO_2 emissions time series, the pink envelope spans a wide range, broadly capturing the decreasing trend and range of values.

Predicted radial displacements between 14 October 2004 and 20 July 2005 mostly follow the observations, particularly at the continuous GPS stations (Figure 5d(ii)). Ra-

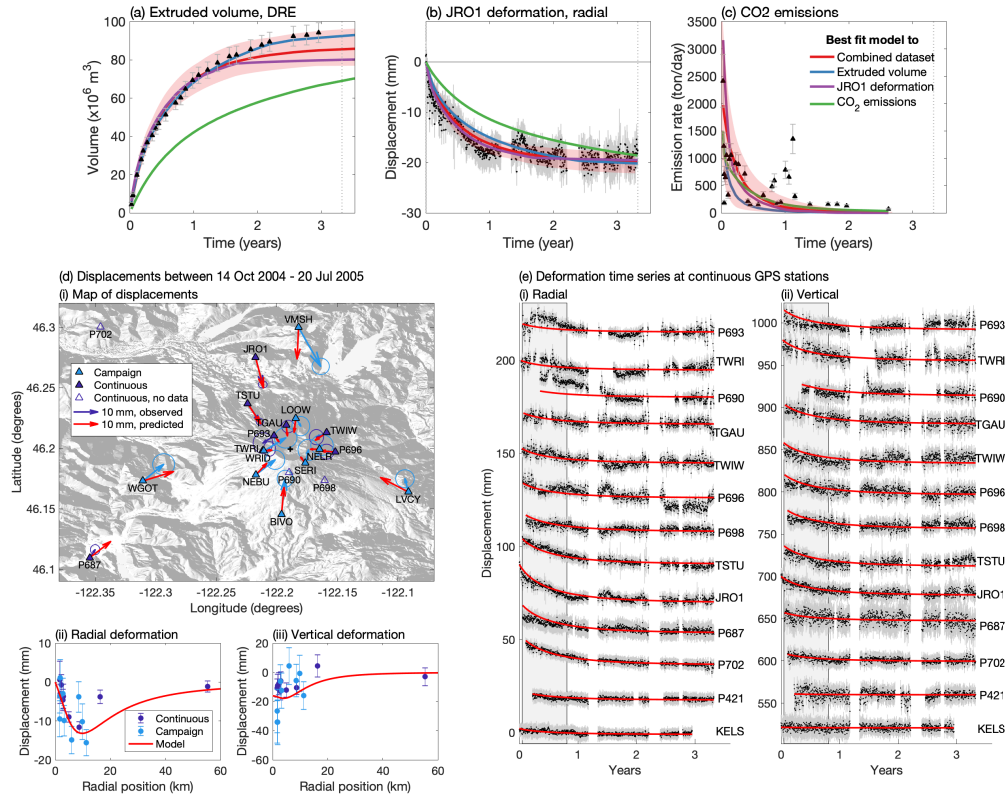


Figure 5. Best-fit model to the combined dataset (red line) compared to observations. (a) Extruded volume, (b) JRO1 radial displacement and (c) CO₂ emissions time series. For (a-c), the range of the models accepted in the appraisal step (pink area), as well as the best-fit models to individual datasets are also shown. Vertical gray dotted lines indicate the eruption end. (d) Predicted displacements from the best-fit model to the combined dataset, showing the (i) map, (ii) radial displacements and (iii) vertical displacements as functions of radial distance from the crater. (e) Predicted radial and vertical deformation time series at the continuous GPS stations, ordered by closest (P693) to furthest (KELS) from the crater. Vertical gray rectangle indicates the time period of the two campaigns. Gaps in the time series occur during slow slip events.

457 dial displacements at the campaign stations are noisier but follow the same general trend.
 458 Fits to vertical deformation during this time are poorer. Campaign stations WRID, NELR
 459 and SERI experienced large vertical displacements (light blue points between -20 and
 460 -40 mm in Figure 5d(iii)) that are likely caused by seasonal effects such as snow accu-
 461 mulation because these stations are at high elevation. The rest of the vertical deforma-
 462 tion data suggest that the maximum should be offset from the crater center (where ra-
 463 dius is zero), supporting a prolate ellipsoid model for the chamber (Yang et al., 1988).
 464 This same model also fits the deformation time series at the continuous GPS stations.

465 Compared to the best-fit models to individual datasets, the best 1000 models to
 466 the combined dataset cannot match each observation as well (Figure 5a-c). Some pen-
 467 alization of fit is needed. For example, the best-fit model to the JRO1 deformation (pur-
 468 ple line) better captures the initial rapid deflation which flattens out after 1 year. How-
 469 ever, this trend yields poor fits to the observed extruded volume both in magnitude and
 470 temporal trend. In order to simultaneously fit the GPS and extruded volume time se-
 471 ries, the search finds models that have slightly poorer fit to the initial rapid deflation at
 472 JRO1. Similarly, the best-fit model to the combined dataset has a distinctively differ-
 473 ent trend compared to the best-fit model to the CO₂ emissions (green line), which pro-
 474 duces a significantly poorer fit to the other datasets.

475 3.2 Posterior probabilities of model parameters

476 We appraise the ensemble of models to generate posterior probability density func-
 477 tions (PDFs) of the model parameters by converting misfits to likelihoods (equation 16,
 478 Figure 6). For comparison, we also calculate the likelihoods given only extruded volume,
 479 only deformation, and the combination of extruded volume and deformation from the
 480 ensemble, and appraise the result. For these appraisals, we also apply the constraints
 481 on dome porosity and zero final extrusion flux.

482 In general, when more datasets are used, the marginal posterior PDFs show tighter
 483 constraints on the model parameters as expected. The extruded volume time series con-
 484 strains the chamber volume, conduit radius, nominal friction coefficient, excess pressure,
 485 magma permeability scale and total volatile contents (Figure 6a). Total extruded vol-
 486 ume scales as $(\beta_{\text{mag}} + \beta_{\text{ch}})\Delta p_{\text{ch}}V_0$ (Segall, 2013) and therefore can offer constraints on
 487 chamber volume given estimates on compressibility which depends on the exsolved volatile
 488 content. The extrusion rate can help to constrain the exsolved volatile content, as a higher
 489 exsolved volatile content would decrease bulk density and enable faster magma ascent.
 490 However, this relationship may not be unique as the extrusion rate is also affected by
 491 the driving pressure, rate of gas escape and frictional resistance.

492 Deformation data alone improves constraints on chamber properties (aspect ratio,
 493 volume, conduit length which controls chamber centroid depth, excess pressure), but volatile
 494 content and frictional properties are poorly constrained (Figure 6b). When extruded vol-
 495 ume and deformation are jointly analyzed, the distributions on all the model parame-
 496 ters except the frictional properties become narrower (Figure 6c). This estimation is en-
 497 hanced by inclusion of CO₂ emissions data in the appraisal. Naturally, the distribution
 498 on chamber CO₂ content is tighter and slightly lower than estimated in the other three
 499 appraisals. This lower volatile content may explain the slightly lower nominal friction
 500 coefficient: a decrease in magma buoyancy requires a corresponding decrease in flow re-
 501 sistance.

502 In all four ensemble appraisals, the magma permeability scale is well constrained
 503 to be above 10⁻¹⁶ m², with all four distributions having approximately similar widths.
 504 This indicates that dome porosity data, which is common to all four appraisals, is the
 505 main control on magma permeability scale. In order for the dome porosity to remain un-
 506 der 40%, magma permeability has to be high enough to allow volatiles to escape from
 507 the conduit.

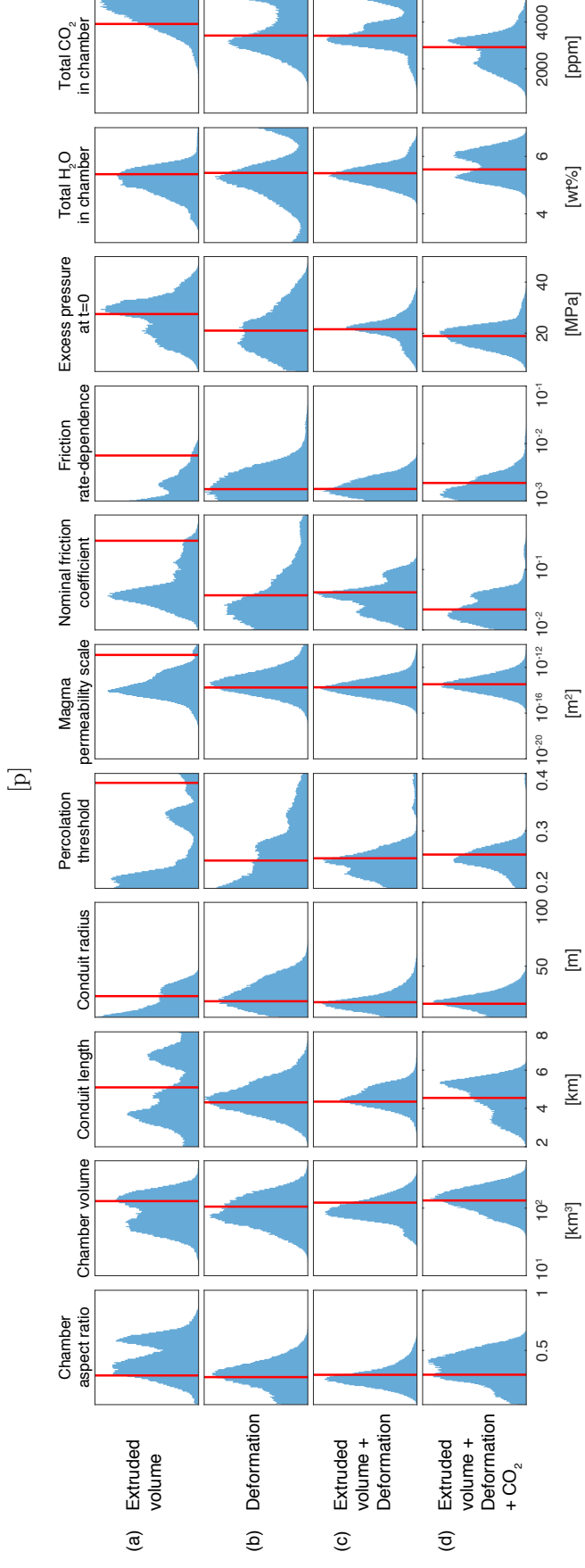


Figure 6. Marginal posterior PDFs of the model parameters when the appraisal is constrained by different datasets. Top row uses extruded volume time series only; middle row uses continuous and campaign GPS data, while the bottom row uses all datasets. Limits of the horizontal axis correspond to the bounds of the uniform prior. Vertical red lines denote the highest likelihood models for each appraisal.

508 In the following sections, we analyze the results of the appraisal by looking at sub-
 509 sets of parameters. Any quoted ranges of parameter values are the 90% credible inter-
 510 vals of the posterior PDF.

511 3.2.1 Chamber properties

512 The preferred chamber volume lies between $64.1 - 256 \text{ km}^3$ (Figure 7a), well be-
 513 low the threshold that indicates that the chamber evolution timescale is comparable to
 514 the ascent timescale. This implies that steady-state solutions are poor approximations
 515 to the temporal evolution of the system, which requires the full time-dependent govern-
 516 ing equations (Wong & Segall, 2019). The data prefer an elongate chamber with an as-
 517 pect ratio (width/height) of $0.13 - 0.55$ with its top (equivalent to conduit length) lo-
 518 cated at $2.95 - 5.79 \text{ km}$ depth. The chamber centroid is located at $9.00 - 17.2 \text{ km}$ depth
 519 with the semi-major axis estimated as $4.59 - 14.0 \text{ km}$. These parameters indicate that
 520 most chambers lie between $5 - 20 \text{ km}$ depth and span about 2 km in width (Figure 7b).

521 The chamber geometry parameters are highly correlated. Aspect ratio exhibits a
 522 negative correlation with the semi-major axis because of how they affect the chamber
 523 volume: a more elongate chamber requires a longer axis to occupy the same volume. A
 524 more elongate chamber also has to be located deeper. Volume loss in the chamber, which
 525 ranges between 20.0 and $66.2 \times 10^6 \text{ m}^3$, exhibits a positive correlation with volume and
 526 centroid depth. Pressure at the conduit base ranges from $80.6 - 144.4 \text{ MPa}$ and is highly
 527 correlated with conduit length to ensure that magma can be pushed out of the conduit
 528 at a similar velocity. This corresponds to $13.1 - 55.5 \text{ MPa}$ over magmastic pressure
 529 (weight of magma column) needed to overcome viscous losses and frictional resistance.
 530 Porosity at the conduit base not only depends on the total water content (not shown),
 531 but also the conduit length and pressure at the base of the conduit.

532 3.2.2 Volatiles and permeability

533 Volatile contents in the chamber are well-constrained in the appraisal (Figure 8a,
 534 b). Total H_2O contents of $4.99 - 6.44 \text{ wt\%}$ and CO_2 contents of $1560 - 3891 \text{ ppm}$ are
 535 preferred. These volatile contents are partitioned into dissolved and exsolved components.
 536 Dissolved H_2O encompasses the relatively common $3.34 - 4.65 \text{ wt\%}$ for arc magmas (Plank
 537 et al., 2013), while dissolved CO_2 is estimated to be $22.0 - 100.3 \text{ ppm}$. Together, these
 538 imply a substantial exsolved phase occupying $5.3 - 16.6\%$ volume fraction at the base
 539 of the conduit. This corresponds to a magma compressibility of $0.20 - 2.67 \times 10^{-10} \text{ Pa}^{-1}$.
 540 Chamber compressibility, which depends on the shape of the chamber and elastic mod-
 541 ulus of the crust (here 20 GPa), has a very narrow range, thus magma compressibility
 542 largely controls the total compressibility which ranges from $0.69 - 3.09 \times 10^{-10} \text{ Pa}^{-1}$.

543 The exsolved phase may be lost through permeable gas escape, both vertically through
 544 the conduit column and laterally through the conduit walls. The magma permeability
 545 scale is well constrained at $1.84 \times 10^{-15} - 7.23 \times 10^{-13} \text{ m}^2$, and the percolation thresh-
 546 old is $0.21 - 0.28$. Vertical gas escape only depends on the magma permeability and ranges
 547 between $8.20 \times 10^{-18} - 2.36 \times 10^{-15} \text{ m}^2$. Lateral gas escape depends on the magma
 548 and wall-rock permeability. However, at the percolation threshold, wall rock permeabil-
 549 ity spans a narrow range of $1.08 - 2.21 \times 10^{-15} \text{ m}^2$ and is generally higher than magma
 550 permeability. Magma permeability is thus the limiting factor for lateral gas escape. This
 551 causes the distribution for both permeabilities to be approximately equal.

552 3.2.3 Conduit friction

553 Extruded volume is the main control on conduit friction due to its relationship with
 554 extrusion rate (Figure 6). In contrast, ensemble appraisal using only the deformation dataset
 555 produces broader distributions on both frictional parameters. When combining extruded

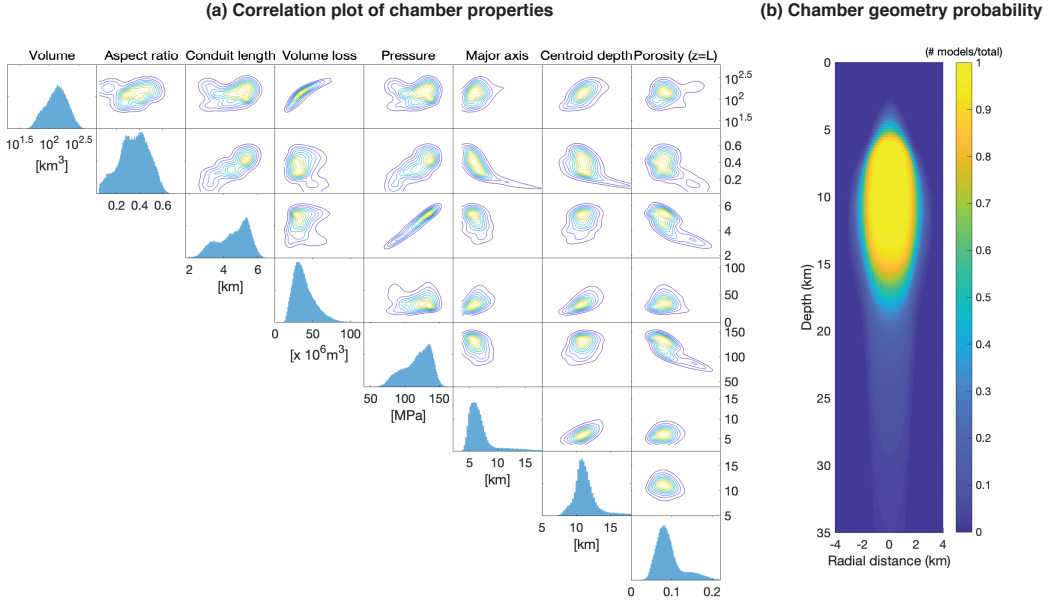


Figure 7. Chamber properties constrained in the appraisal that considers the likelihood of all the datasets. (a) Correlation plot of the chamber properties. Volume, aspect ratio and conduit length are directly estimated, while volume loss, pressure (measured at the chamber top), semi-major axis, centroid depth and porosity (measured at the chamber top) are dependent parameters. (b) 2D slice of the crust showing the probability of finding a chamber at a certain depth and radial distance from the Mount St. Helens edifice. Colors indicate the number of models relative to the total.

volume and deformation data, posterior probabilities of friction become narrower. Since predicted gas emissions depend on the pressure gradient in the plug which is affected by frictional resistance, the ensemble appraisal with all datasets results in a well-constrained nominal frictional coefficient. The marginal posterior PDFs suggest that the nominal friction coefficient is low ($10^{-1.94} - 10^{-1.26}$), while the rate-dependence of friction ranges between $10^{-2.97} - 10^{-2.37}$. This corresponds to friction coefficients between 0.014–0.057 at the reference velocity $v = v_r = 10^{-5}$ m/s (Figure 9). Shear stress is given by $f\sigma_c$ where σ_c is the effective normal stress. At the plug depth (0.76–0.96 km), shear stress ranges between 0.23 – 0.82 MPa.

4 Discussion

Traditional geodetic inversions have used continuous and campaign GPS data from the Mount St. Helens 2004 - 2008 eruption to constrain the geometry and volume change of the chamber (Lisowski et al., 2008; Palano et al., 2012). Using a source model of three colocated orthogonal point cracks, Lisowski et al. (2008) obtain a chamber with an aspect ratio of 0.66 centered at 7.99 km depth with a volume change of 11.9 million m^3 in the first year of eruption. Applying the Yang et al. (1988) model for ellipsoidal chambers, Palano et al. (2012) found a more elongated chamber with aspect ratio 0.10 at a similar depth with a volume change of 7.97 million m^3 in the first two years of the eruption. Notably, the discrepancy in aspect ratio between the two studies arises from the difference in source model, as the predicted spatial pattern of deformation are approximately the same in both studies.

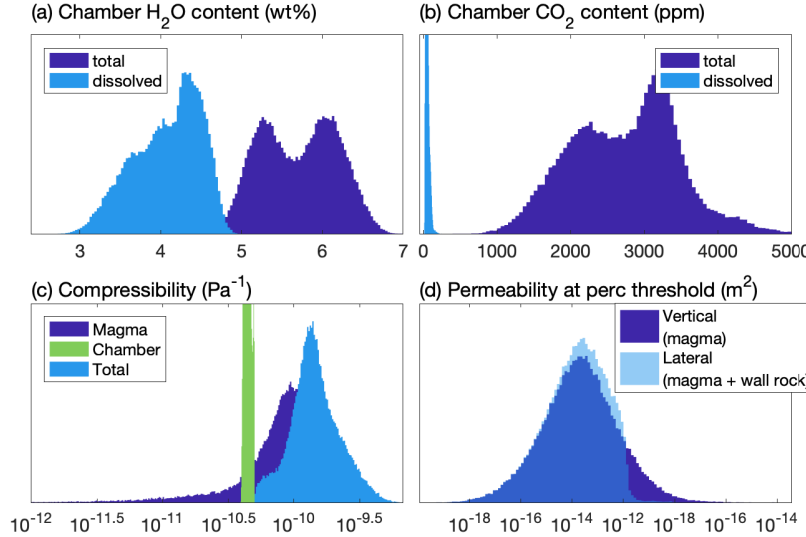


Figure 8. Posterior PDFs of (a) total and dissolved H_2O content in the chamber, (b) total and dissolved CO_2 content in the chamber (note low dissolved content), (c) magma compressibility in the chamber and the chamber compressibility, and (d) vertical and lateral permeability at the percolation threshold depth.

In this study, we applied the source model from Yang et al. (1988) as it satisfies the free surface boundary condition and, in the limit where the chamber is deep relative to the chamber dimensions, the pressure boundary condition on the chamber walls. Therefore our results align more closely with Palano et al. (2012) to prefer a more elongate chamber. The highest likelihood chamber has an aspect ratio of 0.30 with a volume change of 35.8 million m^3 over the whole eruption. The chamber centroid is located at 11.2 km depth. The volume change estimated in this inversion is about 3–4 times larger than Lisowski et al. (2008) and Palano et al. (2012) respectively due to both the longer time interval considered and also the deeper centroid location (Figure 7a). The top of the chamber, located at 4.55 km, has a pressure of 121.4 MPa. This agrees with petrologic constraints, which find that plagioclase phenocrysts continued to grow until pressure decreased to 130 MPa (corresponding to 5 km depth) when magma exits the chamber and enters the conduit (?; Pallister et al., 2008).

Incorporating a physics-based model and extrusion volume data enables us to resolve pressure change and chamber volume, which traditional geodetic inversions are unable to do. Although Palano et al. (2012) obtained a plausible volume change, their preferred model has a pressure change of 1000 MPa and a chamber of volume of only 0.306 km^3 . This large pressure change is inconsistent with the tensile strength of rock which is on the order of 10 MPa. Using a physics-based model with extrusion flux and deformation data, (Anderson & Segall, 2013) modeled a pressure change of 2–10 MPa over the course of the eruption. Combined with the volume change of 16–40 million m^3 constrained by deformation, they estimate the chamber to be at least 40 km^3 and reaching the upper bound of the inversion at 200 km^3 . In this study, the 90% credible interval of the resampled models have pressure change 2–18 MPa and volume loss 16–40 million m^3 , implying a chamber volume of 64–256 km^3 . Total extruded volume scales as $(\beta_{\text{mag}} + \beta_{\text{ch}})\Delta p_{\text{ch}}V_0$ (Segall, 2013). Given the final extrusion volume of 94.2 million m^3 and typical system compressibility of $0.69\text{--}3.09 \times 10^{-10} \text{ Pa}^{-1}$, this implies a chamber volume on the order of 10^2 km^3 , consistent with our posterior PDFs. A similar analysis in Mastin

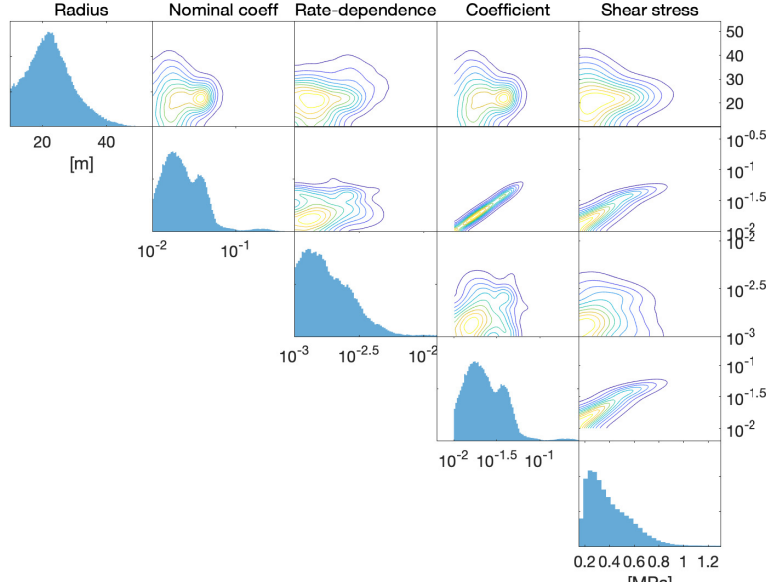


Figure 9. Correlation plots of frictional parameters. Conduit radius, nominal coefficient and rate-dependence are directly estimated, while the friction coefficient at the reference velocity $v = v_r = 10^{-5}$ m/s and shear stress are dependent parameters.

et al. (2009) obtained a smaller chamber volume estimate of 10–25 km³ by using a similar pressure change but 4 – 5 times higher magma compressibility. This difference in compressibility arises because Mastin et al. (2009) used a fixed crystal volume in the chamber, while we include the increase in density due to crystallization, which counteracts some of the decrease in density caused by gas exsolution and expansion. As a result, compressibilities obtained in this study are smaller.

Independent estimates of chamber volume at Mount St. Helens span a wide range from a few km³ to 1000 km³. Eruption volumes can offer a lower bound on chamber size. The largest plinian eruption in the Holocene produced 4 km³ of material (Carey et al., 1995). However, given that Mount St. Helens has more frequently produced lava flows and domes, the more common eruption volume is smaller (Clynne et al., 2008; Pallister et al., 2017). Earthquake hypocenters in the 1980s show distinct lobes surrounding an earthquake-free zone, thought to be the semi-liquid magma body, of about 10 – 20 km³ (Scandone & Malone, 1985). Recent seismic tomography in the iMUSH experiment found a body with low shear wave velocities at 4 – 13 km depth and spanning 15 km wide, corresponding to a volume 1000 km³ (Kiser et al., 2016). Our inversions agree with the vertical extent of the chamber but suggest a more limited horizontal extent. This volume is an upper bound due to resolution limitations. In addition, the melt fraction causing the reduction in shear wave velocities is uncertain. Petrologic evidence of compositionally diverse magma batches with different stagnation depths suggests that volume estimated the iMUSH experiment may reflect a mush containing distinct regions of high melt fraction (Leeman & Smith, 2018; Wanke, Clynne, et al., 2019; Wanke, Karakas, & Bachmann, 2019). This would be consistent with geologic evidence of smaller eruption volumes. Reconciling the discrepancy between our inversion results and the geologic perspective would require more realistic geodetic source models for an mush system containing distinct high melt fraction bodies.

Gas solubility modeling using VolatileCalc (Newman & Lowenstern, 2002) constrained by carbon dioxide emissions and extruded volume give 4.4 wt% dissolved H₂O and 37

633 ppm dissolved CO₂ at 130 MPa, the pressure at the top of the magma chamber assumed
 634 at 5 km depth (Gerlach et al., 2008). This is consistent with inversion estimates of 3.34–
 635 4.65 wt% dissolved H₂O and 22.0–100.3 ppm dissolved CO₂. The same gas solubility mod-
 636 eling suggests a porosity 10.11–10.85% at 130 MPa (Gerlach et al., 2008). At similar
 637 pressures, our inversion results give a porosity of 5.5–10.5%. There are some models
 638 with higher porosities at the conduit base (up to 20%), but these have shorter conduit
 639 lengths and their conduit base pressure is lower, allowing gas to exsolve and expand.

640 Melt inclusions in amphiboles and plagioclase suggest dissolved H₂O contents up
 641 to 3.6 wt%, however most are below 3 wt% which is considered low for the magma equi-
 642 libration pressure of 130 MPa (Blundy et al., 2008; Pallister et al., 2008). This suggests
 643 that melt inclusions may have ruptured or crystallized during ascent and might not be
 644 representative of the actual dissolved water content in the chamber (Blundy et al., 2008;
 645 Pallister et al., 2008; ?, ?). Our inversions, which give dissolved water contents above 3
 646 wt%, supports this interpretation.

647 The magma permeability scale k_c controls the balance between chamber volatile
 648 contents and observed dome porosity, because the distribution of k_c remains consistent
 649 across all four appraisals. This behavior is consistent with inversions using the steady-
 650 state version of this conduit flow model (Wong et al., 2017). However, Wong et al. (2017)
 651 found a tight constraint on $k_c \sim 10^{-12.3} - 10^{-10.5}$ m², while the distribution derived
 652 here finds lower k_c . We attribute this difference to the steady-state assumption as dis-
 653 cussed in Section 4.3 of Wong and Segall (2019). Since each steady-state solution is in-
 654 dependent, the solution adjusts to ensure that magma and gas flux into the region above
 655 the percolation threshold is sufficient to sustain gas escape. The magma column remains
 656 gas-rich even with extensive gas escape due to high permeability allowing extensive gas
 657 ascent. In time-dependent solutions, however, high magma permeability allows a large
 658 proportion of volatiles to be lost to the surroundings at early time to substantially de-
 659 crease the amount of gas in the shallow conduit. This causes the eruption velocity to slow
 660 down drastically which is inconsistent with the extrusion volume time series. Therefore
 661 this high permeability constant is no longer preferred. Instead, an intermediate value that
 662 allows only moderate gas escape is preferred.

663 Laboratory measurements of permeability in the Mount St. Helens plug found ver-
 664 tical permeability of 10⁻¹⁴ m² in the margins and 10⁻¹⁵ m² in the core of the lava dome
 665 (Gaunt et al., 2014). Horizontal permeability was found to be 10⁻¹⁸ m² in the margins
 666 and 10⁻¹⁵ m² in the core (Gaunt et al., 2014). Our modeled permeability captures this
 667 range of values with few models having permeability greater than 10⁻¹⁴ m², although
 668 it does not account for the anisotropy observed in the experiments. Two-dimensional nu-
 669 matical models suggest that at shallow depths, gases tend to concentrate near the con-
 670 duct margins which enhances gas escape (Collombet, 2009). This is corroborated by ring-
 671 shaped degassing observations at Santiaguito volcano in Guatemala (Bluth & Rose, 2004).

672 Furthermore, we do not consider the impact of crystals on gas percolation in equa-
 673 tion 9. Experiments have shown that the presence of crystals can enhance bubble nu-
 674 cleation and control bubble size (Belien et al., 2010; Spina et al., 2016). Channelization
 675 of gas flow may occur at high crystal contents particularly in magmas with elongated
 676 crystals, leading to efficient gas migration (Oppenheimer et al., 2015; Spina et al., 2016).
 677 Higher-dimensional, pore-scale simulations better capture this spatially localized mode
 678 of degassing (Parmigiani et al., 2016; Degruyter et al., 2019). In contrast, this study fo-
 679 cuses on the macro-scale impact of gas escape on extrusion flux, ground deformation and
 680 gas emissions, which are unable to resolve the spatial heterogeneity of gas flow.

681 Inversion results suggest a narrow conduit of radius 11.9 – 35.8 m. Previous in-
 682 versions with the steady-state conduit model used linear extrusion rates observed by re-
 683 mote cameras (Major et al., 2008) and extrusion flux to estimate the conduit radius, giv-
 684 ing a best-fit radius of 148 m (Wong et al., 2017). Deformation was not included as a

constraint in Wong et al. (2017). In this inversion, we omitted the linear extrusion rate as a constraint because it may only reflect the near-surface conduit geometry. Flaring conduit geometries have been seen in the rare cases where we have camera observations a few 100 meters into conduits (Lyons et al., 2016; Moussallam et al., 2016; Johnson et al., 2018). Mechanical modeling also shows that conduit collapse during explosive eruptions can create the flared geometry at the top (Macedonio et al., 1994; Mitchell, 2005; Aravena et al., 2017). Therefore including the linear extrusion rate would have biased results towards conduit radii larger than the average radius of the conduit.

Information from the amplitude and temporal evolution of observations provides the constraint on radius, as seen in sensitivity analyses of Wong and Segall (2019). When holding all other parameters constant, doubling conduit radius would increase the magma velocity and mass flow rate by 4 and 16 times respectively. The rate of pressure evolution, which is proportional to mass flow rate (equation 10), will also increase by 16 times. To maintain the same mass flow rate, we would need to reduce the chamber pressure, but this would cause the total extruded volume and radial displacements to decrease which would reduce the fit to observations. In addition, chamber pressure cannot decrease by 16 times, as it would cause the magma to be underpressured. Chamber volumes considered here could vary by that extent, however it would alter the relative magnitudes of extruded volume and radial displacements. The conduit radii of 11.9–35.8 m balance these competing effects to ensure fit to the data.

The smaller radius may also explain the higher pressure over magmastic and the lower friction coefficient estimated here compared to the distribution obtained from the steady-state model. Previous inversions using the steady-state conduit model already estimated low f_0 (10^{-2} – $10^{-0.25}$), with the maximum *a posteriori* model having $f_0 = 0.46$ (Wong et al., 2017). The conduit model only resolves shear stress on the conduit walls $\tau_R = f(\sigma - p_{\text{hyd}})$, where the normal stress σ was assumed to be lithostatic and the pore pressure p_{hyd} was assumed to be hydrostatic. Decreasing σ by considering topographic or tectonic effects could result in higher estimated f_0 . Elevated pore pressures due to gases escaping laterally and localizing on the conduit margins may also increase the estimated f_0 . Even so, the f_0 estimated in this study are lower than in (Wong et al., 2017), suggesting that other reasons, such as the narrower conduit, must cause the low friction estimated in inversions using the time-dependent model. A narrower conduit has a higher ratio of surface area to cross-sectional area. To maintain the same flow rate, we would need to increase the driving force for flow, or reduce the viscous and/or frictional losses. The slight positive correlation between radius and the nominal friction coefficient (Figure 9) suggests that within the limited range of radii that fit the data, the friction coefficient is lower for narrower conduits. The weak relationship implies that other parameters trade off with friction coefficient. Of course, inaccuracies in the model for magma viscosity will trade off with estimates of the frictional resistance. Viscosity models with reduced dependence on the crystal fraction compared to the Costa (2005) model would reduce viscous losses, and therefore require greater frictional losses and hence a a higher friction coefficient to achieve the same mass flow rate.

5 Conclusion

In this study, we applied a simple physics-based model to estimate critical properties of the magmatic system at Mount St. Helens based on diverse time series data from the 2004–2008 eruption. The model takes into account pressure-dependent crystallization, volatile exsolution and gas escape during magma ascent. These processes cause magma flowing viscously at depth to transition to solid plug sliding at shallow depth, ultimately extruding a dome in the crater. To constrain important parameters in the model, we jointly apply extruded volume, continuous and campaign GPS positions and carbon dioxide emissions time series from the eruption in an inversion using the neighborhood algorithm (Sambridge, 1999b, 1999a).

737 Key findings of the inversion include:

- 738 1. We are able to find models that fit the extruded volume, ground deformation and
739 carbon dioxide emissions from the 2004–2008 eruption at Mount St. Helens. In par-
740 ticular, the best-fit model approximately captures the rapid decay in JRO1 radial
741 displacement while maintaining satisfactory fits to the other datasets, which pre-
742 vious studies were unable to replicate.
- 743 2. The data prefer elongate chambers with aspect ratios 0.13–0.55, located at 9.00–
744 17.2 km depth with chamber volumes between 64.1 – 256 km³. These chamber
745 volumes suggest that solutions to the full time-dependent governing equations is
746 needed to model the temporal evolution of the eruption. Volume lost from the cham-
747 ber is 20 – 66 million m³.
- 748 3. The top of the chamber has total (dissolved and exsolved) water contents of 4.99–
749 6.44 wt% and carbon dioxide contents of 1560–3891 ppm. At 130 MPa, which
750 is the top of the magma chamber inferred from plagioclase phase equilibrium, this
751 corresponds to a porosity of 5.5–10%.
- 752 4. Excess exsolved volatiles to escape the system vertically through the conduit and
753 laterally through the conduit walls. The magma permeability scale is well-constrained
754 by the porosity of dome rock.
- 755 5. Compared to previous inversions using the steady-state conduit model (Wong et
756 al., 2017), this inversion using the time-dependent model suggests a lower magma
757 permeability scale because of differences in the mechanism for gas escape in steady-
758 state and time-dependent conduit flow models. In addition, a narrower conduit
759 of radius 11.9–35.8 m is preferred. This may account for the higher pressure over
760 magmastic (13.1–55.5 MPa) and lower conduit wall friction coefficients (0.014–
761 0.057 at the reference velocity $v = v_r = 10^{-5}$ m/s). A weaker dependence of
762 viscosity on crystal fraction would allow larger friction coefficients.

763 Acknowledgments

764 This study was supported by the National Science Foundation (NSF) [10.13039/100000001]
765 EAR-1358607. Code used and developed in this study are available here: conduit model
766 (<http://doi.org/10.5281/zenodo.3969094>), parameter estimation (<http://doi.org/10.5281/zenodo.3969103>), inversions for Mount St. Helens (<http://doi.org/10.5281/zenodo.3969090>), inversion results files (<http://doi.org/10.5281/zenodo.3969105>).
767 Data from the Mount St. Helens eruption are available from Schilling et al. (2008), Lisowski
768 et al. (2008), Gerlach et al. (2008) and Dzurisin et al. (2015), as well as the USGS Pa-
769 cific Northwest GPS Network (https://earthquake.usgs.gov/monitoring/gps/Pacific_Northwest). We are grateful to Michael Lisowski for help in processing the GPS data.
770

773 References

- 774 Albino, F., Pinel, V., Massol, H., & Collombet, M. (2011). Conditions for detection
775 of ground deformation induced by conduit flow and evolution. *Journal of Geo-
776 physical Research: Solid Earth*, 116(6), 1–18. doi: 10.1029/2010JB007871
- 777 Amoruso, A., & Crescentini, L. (2009). Shape and volume change of pressurized
778 ellipsoidal cavities from deformation and seismic data. *Journal of Geophysical
779 Research: Solid Earth*, 114(2), 1–8. doi: 10.1029/2008JB005946
- 780 Anderson, K., Lisowski, M., & Segall, P. (2010). Cyclic ground tilt associated with
781 the 2004–2008 eruption of Mount St. Helens. *Journal of Geophysical Research:
782 Solid Earth*, 115(11), 1–29. doi: 10.1029/2009JB007102
- 783 Anderson, K., & Segall, P. (2011). Physics-based models of ground deformation
784 and extrusion rate at effusively erupting volcanoes. *Journal of Geophysical Re-
785 search: Solid Earth*, 116(7), 1–20. doi: 10.1029/2010JB007939
- 786 Anderson, K., & Segall, P. (2013). Bayesian inversion of data from effusive volcanic

- 787 eruptions using physics-based models: Application to Mount St. Helens 2004-
 788 2008. *Journal of Geophysical Research: Solid Earth*, 118(5), 2017–2037. doi:
 789 10.1002/jgrb.50169
- 790 Aravena, A., de'Michieli Vitturi, M., Cioni, R., & Neri, A. (2017). Stability of vol-
 791 canic conduits during explosive eruptions. *Journal of Volcanology and Geother-
 792 mal Research*. Retrieved from [http://linkinghub.elsevier.com/retrieve/
 793 pii/S0377027317301427](http://linkinghub.elsevier.com/retrieve/pii/S0377027317301427) doi: 10.1016/j.jvolgeores.2017.05.003
- 794 Belien, I. B., Cashman, K. V., & Rempel, A. W. (2010). Gas accumulation in
 795 particle-rich suspensions and implications for bubble populations in crystal-
 796 rich magma. *Earth and Planetary Science Letters*, 297(1-2), 133–140. Re-
 797 trieval from <http://dx.doi.org/10.1016/j.epsl.2010.06.014> doi:
 798 10.1016/j.epsl.2010.06.014
- 799 Blower, J. (2001). Factors controlling permeability-porosity relationships in magma.
 800 *Bulletin of Volcanology*, 63, 497–504. doi: 10.1007/s004450100172
- 801 Blundy, J., Cashman, K. V., & Berlo, K. (2008). Evolving magma storage conditions
 802 beneath Mount St. Helens inferred from chemical variations in melt inclusions
 803 from the 1980-1986 and current (2004-2006) eruptions. *A Volcano Rekindled: The
 804 Renewed Eruption of Mount St. Helens 2004-2006, U.S. Geological Survey Profes-
 805 sional Paper 1750*, 755–790. Retrieved from <http://www.scopus.com/inward/record.url?eid=2-s2.0-84864213506&partnerID=40&md5=882e27194e3279f6c7076734494e88d8>
- 806 Bluth, G. J., & Rose, W. I. (2004). Observations of eruptive activity at Santiaguito
 807 volcano, Guatemala. *Journal of Volcanology and Geothermal Research*, 136(3-4),
 808 297–302. doi: 10.1016/j.jvolgeores.2004.06.001
- 809 Carey, S., Gardner, J., & Sigurdsson, H. (1995). The intensity and magni-
 810 tude of Holocene plinian eruptions from Mount St. Helens volcano. *Journal of
 811 Volcanology and Geothermal Research*, 66(1-4), 185–202. doi:
 812 10.1016/0377-0273(94)00059-P
- 813 Caricchi, L., Burlini, L., Ulmer, P., Gerya, T., Vassalli, M., & Papale, P. (2007).
 814 Non-Newtonian rheology of crystal-bearing magmas and implications for
 815 magma ascent dynamics. *Earth and Planetary Science Letters*, 264(3-4),
 816 402–419. doi: 10.1016/j.epsl.2007.09.032
- 817 Cashman, K. V., Thornber, C., & Pallister, J. S. (2008). From Dome to Dust:
 818 Shallow Crystallization and Fragmentation of Conduit Magma During the
 819 2004-2006 Dome Extrusion of Mount St. Helens, Washington. *A Vol-
 820 cano Rekindled: The Renewed Eruption of Mount St. Helens 2004-2006,
 821 U.S. Geological Survey Professional Paper 1750*, 387–413. Retrieved from
 822 <http://cat.inist.fr/?aModele=afficheN&cpsidt=22527815>
- 823 Clyne, M. A., Calvert, A. T., Wolfe, E. W., Evarts, R. C., Fleck, R. J., & Lan-
 824 phere, M. A. (2008). The pleistocene eruptive history of Mount St. Helens,
 825 Washington, from 300,000 to 12,800 years before present. *US Geological Survey
 826 Professional Paper*(1750), 593–628. doi: 10.3133/pp175028
- 827 Collombet, M. (2009). Two-dimensional gas loss for silicic magma flows: Toward
 828 more realistic numerical models. *Geophysical Journal International*, 177(1),
 829 309–318. doi: 10.1111/j.1365-246X.2008.04086.x
- 830 Costa, A. (2005). Viscosity of high crystal content melts: Dependence on solid frac-
 831 tion. *Geophysical Research Letters*, 32(22), 1–5. doi: 10.1029/2005GL024303
- 832 Crowell, B. W., Bock, Y., & Liu, Z. (2016). Single-station automated detection
 833 of transient deformation in GPS time series with the relative strength index:
 834 A case study of Cascadian slow slip. *Journal of Geophysical Research: Solid
 835 Earth*, 121(12), 9077–9094. doi: 10.1002/2016JB013542
- 836 De' Michieli Vitturi, M., Clarke, A. B., Neri, A., & Voight, B. (2013). Extrusion
 837 cycles during dome-building eruptions. *Earth and Planetary Science Letters*,
 838 371-372, 37–48. Retrieved from <http://dx.doi.org/10.1016/j.epsl.2013.03.037> doi: 10.1016/j.epsl.2013.03.037

- 842 Degruyter, W., Parmigiani, A., Huber, C., & Bachmann, O. (2019, feb). How do
 843 volatiles escape their shallow magmatic hearth? *Philosophical Transactions
 844 of the Royal Society A: Mathematical, Physical and Engineering Sciences*,
 845 377(2139). Retrieved from <http://www.royalsocietypublishing.org/doi/10.1098/rsta.2018.0017> doi: 10.1098/rsta.2018.0017
- 846 Denlinger, R. P., & Hoblitt, R. P. (1999). Cyclic eruptive behavior of silicic volca-
 847 noes. *Geology*, 27(5), 459–462. doi: 10.1130/0091-7613(1999)027<0459
- 848 Dzurisin, D., Moran, S. C., Lisowski, M., Schilling, S. P., Anderson, K. R., &
 849 Werner, C. (2015). The 2004–2008 dome-building eruption at Mount St.
 850 Helens, Washington: epilogue. *Bulletin of Volcanology*, 77(10), 89. Re-
 851 tried from <http://link.springer.com/10.1007/s00445-015-0973-4> doi:
 852 10.1007/s00445-015-0973-4
- 853 Fukushima, Y., Cayol, V., & Durand, P. (2005). Finding realistic dike models from
 854 interferometric synthetic aperture radar data: The February 2000 eruption at
 855 Piton de la Fournaise. *Journal of Geophysical Research: Solid Earth*, 110(3),
 856 1–15. doi: 10.1029/2004JB003268
- 857 Gaunt, H. E., Sammonds, P. R., Meredith, P. G., Smith, R., & Pallister, J. S.
 858 (2014). Pathways for degassing during the lava dome eruption of Mount
 859 St. Helens 2004–2008. *Geology*, 42(11), 947–950. Retrieved from <http://geology.gsapubs.org/cgi/doi/10.1130/G35940.1> doi: 10.1130/G35940.1
- 860 Gerlach, T. M., Mcgee, K. A., & Doukas, M. P. (2008). Emission Rates of CO₂,
 861 SO₂, and H₂S, Scrubbing, and Preeruption Excess Volatiles at Mount St. He-
 862 lens, 2004–2005. *A Volcano Rekindled: The Renewed Eruption of Mount St.*
 863 *Helens 2004–2006*, U.S. Geological Survey Professional Paper 1750, 543–571.
- 864 Gonnermann, H. M., & Manga, M. (2007). The Fluid Mechanics Inside a Volcano.
 865 *Annual Review of Fluid Mechanics*, 39, 321–356. doi: 10.1146/annurev.fluid.39
 866 .050905.110207
- 867 Iverson, R. M. (2008). Dynamics of Seismogenic Volcanic Extrusion Resisted by a
 868 Solid Surface Plug, Mount St. Helens, 2004–2005. *A Volcano Rekindled: The*
 869 *Renewed Eruption of Mount St. Helens 2004–2006*, U.S. Geological Survey
 870 Professional Paper 1750, 425–460.
- 871 Jaupart, C., & Allègre, C. J. (1991). Gas content, eruption rate and instabilities
 872 of eruption regime in silicic volcanoes. *Earth and Planetary Science Letters*,
 873 102(3-4), 413–429. doi: 10.1016/0012-821X(91)90032-D
- 874 Johnson, J. B., Watson, L. M., Palma, J. L., Dunham, E. M., & Anderson, J. F.
 875 (2018). Forecasting the Eruption of an Open-Vent Volcano Using Resonant
 876 Infrasound Tones. *Geophysical Research Letters*, 45(5), 2213–2220. doi:
 877 10.1002/2017GL076506
- 878 Kawaguchi, R., & Nishimura, T. (2015). Numerical investigation of temporal
 879 changes in volcanic deformation caused by a gas slug ascent in the conduit.
 880 *Journal of Volcanology and Geothermal Research*, 302, 1–10. Retrieved
 881 from <http://dx.doi.org/10.1016/j.jvolgeores.2015.06.002> doi:
 882 10.1016/j.jvolgeores.2015.06.002
- 883 Kiser, E., Palomeras, I., Levander, A., Zelt, C., Harder, S., Schmandt, B., ... Ul-
 884 berg, C. (2016). Magma reservoirs from the upper crust to the Moho
 885 inferred from high-resolution Vp and Vs models beneath Mount St. He-
 886 lens, Washington State, USA. *Geology*, 44(6), G37591.1. Retrieved from
 887 <http://geology.gsapubs.org/lookup/doi/10.1130/G37591.1> doi:
 888 10.1130/G37591.1
- 889 Klug, C., & Cashman, K. V. (1996). Permeability development in vesiculating mag-
 890 mas: implications for fragmentation. *Bulletin of Volcanology*, 58, 87–100. doi:
 891 10.1007/s004450050128
- 892 Kozono, T., & Koyaguchi, T. (2012). Effects of gas escape and crystallization
 893 on the complexity of conduit flow dynamics during lava dome eruptions.
 894 *Journal of Geophysical Research: Solid Earth*, 117(March), 1–18. doi:

- 897 10.1029/2012JB009343
- 898 Langbein, J. (2004). Noise in two-color electronic distance meter measurements re-
899 visited. *Journal of Geophysical Research: Solid Earth*, *109*(4), 1–16. doi: 10
900 .1029/2003JB002819
- 901 Leeman, W. P., & Smith, D. R. (2018). The role of magma mixing, identifica-
902 tion of mafic magma inputs, and structure of the underlying magmatic sys-
903 tem at Mount St. Helens. *American Mineralogist*, *103*(12), 1925–1944. doi:
904 10.2138/am-2018-6555
- 905 Lisowski, M., Dzurisin, D., Denlinger, R. P., & Iwatsubo, E. Y. (2008). Analysis
906 of GPS-Measured Deformation Associated with the 2004–2006 Dome-Building
907 Eruption of Mount St. Helens, Washington. *A Volcano Rekindled: The Re-
908 newed Eruption of Mount St. Helens 2004–2006, U.S. Geological Survey Profes-
909 sional Paper 1750*, 301–333.
- 910 Liu, Y., Zhang, Y., & Behrens, H. (2005). Solubility of H₂O in rhyolitic melts at low
911 pressures and a new empirical model for mixed H₂O-CO₂ solubility in rhyolitic
912 melts. *Journal of Volcanology and Geothermal Research*, *143*(1-3), 219–235.
913 doi: 10.1016/j.jvolgeores.2004.09.019
- 914 Llewellyn, E. W., & Manga, M. (2005). Bubble suspension rheology and implications
915 for conduit flow. *Journal of Volcanology and Geothermal Research*, *143*(1-3),
916 205–217. doi: 10.1016/j.jvolgeores.2004.09.018
- 917 Lyons, J. J., Haney, M. M., Werner, C., Kelly, P., Patrick, M., Kern, C., & Trus-
918 dell, F. (2016, jan). Long period seismicity and very long period infra-
919 sound driven by shallow magmatic degassing at Mount Pagan, Mariana
920 Islands. *Journal of Geophysical Research: Solid Earth*, *121*(1), 188–209.
921 Retrieved from <http://doi.wiley.com/10.1002/2015JB012490> doi:
922 10.1002/2015JB012490
- 923 Macedonio, G., Dobran, F., & Neri, A. (1994, jan). Erosion processes in
924 volcanic conduits and application to the AD 79 eruption of Vesuvius.
925 *Earth and Planetary Science Letters*, *121*(1-2), 137–152. Retrieved from
926 <https://linkinghub.elsevier.com/retrieve/pii/0012821X9490037X> doi:
927 10.1016/0012-821X(94)90037-X
- 928 Major, J. J., Kingsbury, C. G., Poland, M. P., & Lahusen, R. G. (2008). Extrusion
929 Rate of the Mount St. Helens Lava Dome Estimated from Terrestrial Imagery,
930 November 2004December 2005. *A Volcano Rekindled: The Renewed Eruption
931 of Mount St. Helens 2004–2006, U.S. Geological Survey Professional Paper
932 1750*, 237–255.
- 933 Manning, C. E., & Ingebritsen, S. E. (1999). Permeability of the continental crust:
934 Implications of geothermal data and metamorphic systems. *Reviews of Geo-
935 physics*, *37*(1), 127–150.
- 936 Mao, A., Harrison, C. G. A., & Dixon, T. H. (1999, feb). Noise in GPS coordi-
937 nate time series. *Journal of Geophysical Research: Solid Earth*, *104*(B2), 2797–
938 2816. Retrieved from <http://doi.wiley.com/10.1029/1998JB900033> doi: 10
939 .1029/1998JB900033
- 940 Mastin, L. G. (2002). Insights into volcanic conduit flow from an open-source nu-
941 matical model. *Geochemistry, Geophysics, Geosystems*, *3*(7), 1–18.
- 942 Mastin, L. G., Lisowski, M., Roeloffs, E., & Beeler, N. (2009). Improved constraints
943 on the estimated size and volatile content of the Mount St. Helens magma sys-
944 tem from the 2004–2008 history of dome growth and deformation. *Geophysical
945 Research Letters*, *36*, 1–4. doi: 10.1029/2009GL039863
- 946 Melnik, O., & Sparks, R. S. J. (2005). Controls on conduit magma flow dynamics
947 during lava dome building eruptions. *Journal of Geophysical Research B: Solid
948 Earth*, *110*(2), 1–21. doi: 10.1029/2004JB003183
- 949 Mitchell, K. L. (2005). Coupled conduit flow and shape in explosive volcanic erup-
950 tions. *Journal of Volcanology and Geothermal Research*, *143*(1-3), 187–203.
951 doi: 10.1016/j.jvolgeores.2004.09.017

- 952 Moran, S. C., Malone, S. D., Qamar, a. I., Thelen, W. a., Wright, a. K., & Caplan-
 953 Auerbach, J. (2008). Seismicity Associated with Renewed Dome Building
 954 at Mount St. Helens, 2004-2005. *A Volcano Rekindled: The Renewed
 955 Eruption of Mount St. Helens 2004-2006, U.S. Geological Survey Pro-
 956 fessional Paper 1750*, 27-60. Retrieved from <http://cat.inist.fr/?aModele=afficheN&cpsidt=22527798%5Cnpapers2://publication/uuid/B8CC1216-2240-4CDA-B943-F693FBD90597>
- 957 Moussallam, Y., Bani, P., Curtis, A., Barnie, T., Moussallam, M., Peters, N., ...
 958 Cardona, C. (2016). Sustaining persistent lava lakes: Observations from high-
 959 resolution gas measurements at Villarrica volcano, Chile. *Earth and Planetary
 960 Science Letters*, 454, 237-247. Retrieved from <http://dx.doi.org/10.1016/j.epsl.2016.09.012> doi: 10.1016/j.epsl.2016.09.012
- 961 Neuberg, J. W., Collinson, A. S., Mothes, P. A., C. Ruiz, M., & Aguaiza, S. (2018).
 962 Understanding cyclic seismicity and ground deformation patterns at volcanoes:
 963 Intriguing lessons from Tungurahua volcano, Ecuador. *Earth and Planetary
 964 Science Letters*, 482, 193-200. Retrieved from <https://doi.org/10.1016/j.epsl.2017.10.050> doi: 10.1016/j.epsl.2017.10.050
- 965 Newman, S., & Lowenstern, J. B. (2002). Volatile Calc : a silicate melt H₂O CO₂
 966 solution model written in Visual Basic for excel. *Computers & Geosciences*,
 967 28, 597-604. doi: doi:10.1016/S0098-3004(01)00081-4
- 968 Oppenheimer, J., Rust, A. C., Cashman, K. V., & Sandnes, B. (2015). Gas migra-
 969 tion regimes and outgassing in particle-rich suspensions. *Frontiers in Physics*,
 970 3(August), 1-13. Retrieved from <http://journal.frontiersin.org/Article/10.3389/fphy.2015.00060/abstract> doi: 10.3389/fphy.2015.00060
- 971 Palano, M., Guarnera, E., & Mattia, M. (2012). GPS ground deformation pat-
 972 terns at Mount St. Helens (Washington, USA) from 2004 to 2010. *Terra Nova*,
 973 24(2), 148-155. doi: 10.1111/j.1365-3121.2011.01049.x
- 974 Pallister, J. S., Clyne, M. A., Wright, H. M., Eaton, A. R. V., Vallance, J. W.,
 975 Sherrod, D. R., & Kokelaar, B. P. (2017). Field-trip guide to Mount St. He-
 976 lens, Washington - An overview of the eruptive history and petrology, tephra
 977 deposits, 1980 pyroclastic density current deposits, and the crater. *Sci-
 978 entific Investigations Report*, 23. Retrieved from <https://pubs.er.usgs.gov/publication/sir20175022D> doi: 10.3133/sir20175022d
- 979 Pallister, J. S., Thornber, C. R., Cashman, K. V., Clyne, M. a., Lowers, H. a.,
 980 Mandeville, C. W., ... Meeker, G. P. (2008). Petrology of the 2004-2006
 981 Mount St. Helens Lava Dome – Implications for Magmatic Plumbing and
 982 Eruption Triggering. *A Volcano Rekindled: The Renewed Eruption of Mount
 983 St. Helens 2004-2006, U.S. Geological Survey Professional Paper 1750*, 647-
 984 702.
- 985 Papale, P. (2001). Dynamics of magma flow in volcanic conduits with vari-
 986 able fragmentation efficiency and nonequilibrium pumice degassing. *Jour-
 987 nal of Geophysical Research: Solid Earth*, 106(B6), 11043-11065. Re-
 988 trieved from <http://doi.wiley.com/10.1029/2000JB900428> doi:
 989 10.1029/2000JB900428
- 990 Parmigiani, A., Faroughi, S., Huber, C., Bachmann, O., & Su, Y. (2016). Bubble
 991 accumulation and its role in the evolution of magma reservoirs in the upper
 992 crust. *Nature*, 532(7600), 492-495. doi: 10.1038/nature17401
- 993 Plank, T., Kelley, K. a., Zimmer, M. M., Hauri, E. H., & Wallace, P. J. (2013). Why
 994 do mafic arc magmas contain ~4wt% water on average? *Earth and Planetary
 995 Science Letters*, 364, 168-179. Retrieved from <http://dx.doi.org/10.1016/j.epsl.2012.11.044> doi: 10.1016/j.epsl.2012.11.044
- 996 Pritchard, M. E., & Simons, M. (2002). A satellite geodetic survey of large-scale
 997 deformation of volcanic centres in the central Andes. *Nature*, 418(6894), 167-
 998 171. doi: 10.1038/nature00872

- 1007 Rice, J. R., Lapusta, N., & Ranjith, K. (2001). Rate and state dependent
 1008 friction and the stability of sliding between elastically deformable solids.
 1009 *Journal of the Mechanics and Physics of Solids*, 49(9), 1865–1898. doi:
 1010 10.1016/S0022-5096(01)00042-4
- 1011 Saar, M. O., & Manga, M. (1999). Permeability-porosity relationship in
 1012 vesicular basalts. *Geophysical Research Letters*, 26(1), 111–114. doi:
 1013 10.1029/1998GL900256
- 1014 Sambridge, M. (1999a). Geophysical inversion with a neighborhood algorithm - II.
 1015 Appraising the ensemble. *Geophysical Journal International*, 138, 727–746.
- 1016 Sambridge, M. (1999b). Geophysical inversion with a neighbourhood algorithm -
 1017 I. Searching a parameter space. *Geophysical Journal International*, 138, 479–
 1018 494.
- 1019 Scandone, R., & Malone, S. D. (1985). Magma supply, magma discharge
 1020 and readjustment of the feeding system of Mount St. Helens during 1980.
 1021 *Journal of Volcanology and Geothermal Research*, 23(3-4), 239–262. doi:
 1022 10.1016/0377-0273(85)90036-8
- 1023 Schilling, S. P., Thompson, R., Messerich, J., & Iwatsubo, E. Y. (2008). Use of Dig-
 1024 ital Aerophotogrammetry to Determine Rates of Lava Dome Growth, Mount
 1025 St. Helens, Washington, 2004-2005. *A Volcano Rekindled: The Renewed Erup-
 1026 tion of Mount St. Helens 2004-2006, U.S. Geological Survey Professional Paper*
 1027 1750, 145–167.
- 1028 Schneider, A., Rempel, A. W., & Cashman, K. V. (2012). Conduit degassing and
 1029 thermal controls on eruption styles at Mount St. Helens. *Earth and Plane-
 1030 tary Science Letters*, 357-358, 347–354. Retrieved from <http://dx.doi.org/10.1016/j.epsl.2012.09.045> doi: 10.1016/j.epsl.2012.09.045
- 1031 Scott, W. E., Sherrod, D. R., & Gardner, C. A. (2008). Overview of the 2004 to
 1032 2006, and Continuing, Eruption of Mount St. Helens, Washington. *A Vol-
 1033 cano Rekindled: The Renewed Eruption of Mount St. Helens, 2004-2006: US*
 1034 *Geological Survey Professional Paper* 1750 (October 2004), 3–22.
- 1035 Segall, P. (2013). Volcano deformation and eruption forecasting. *Geological So-
 1036 ciety, London, Special Publications*, 380, 85–106. Retrieved from <http://sp.lyellcollection.org/cgi/doi/10.1144/SP380.4> doi: 10.1144/SP380.4
- 1037 Smith, R., Sammonds, P. R., Tuffen, H., & Meredith, P. G. (2011). Evolution
 1038 of the mechanics of the 2004-2008 Mt. St. Helens lava dome with time and
 1039 temperature. *Earth and Planetary Science Letters*, 307(1-2), 191–200. Re-
 1040 trieval from <http://dx.doi.org/10.1016/j.epsl.2011.04.044> doi:
 1041 10.1016/j.epsl.2011.04.044
- 1042 Spina, L., Cimarelli, C., Scheu, B., Di Genova, D., & Dingwell, D. B. (2016). On the
 1043 slow decompressive response of volatile- and crystal-bearing magmas: An ana-
 1044 logue experimental investigation. *Earth and Planetary Science Letters*, 433,
 1045 44–53. Retrieved from <http://dx.doi.org/10.1016/j.epsl.2015.10.029>
 1046 doi: 10.1016/j.epsl.2015.10.029
- 1047 Thornber, C. R., Pallister, J. S., Rowe, M. C., McConnell, S., Herriott, T. M., Eck-
 1048 berg, A., ... Knaack, C. M. (2008). *Catalog of Mount St. Helens 2004-2007
 1049 Dome Samples with Major- and Trace-element Chemistry: U.S. Geological
 1050 Survey Open-File Report 2008-1130* (Tech. Rep.). U.S. Geological Survey.
 1051 Retrieved from <http://pubs.usgs.gov/of/2008/1130/>
- 1052 Vallance, J., Schneider, D., & Schilling, S. (2008). Growth of the 2004-2006 Lava-
 1053 Dome Complex at Mount St. Helens, Washington. *A Volcano Rekindled: The
 1054 Renewed Eruption of Mount St. Helens 2004-2006, U.S. Geological Survey*
 1055 *Professional Paper* 1750, 169–208.
- 1056 Wanke, M., Clyne, M. A., von Quadrt, A., Vennemann, T. W., & Bachmann,
 1057 O. (2019). Geochemical and petrological diversity of mafic magmas from
 1058 Mount St. Helens. *Contributions to Mineralogy and Petrology*, 174(1), 1–
 1059 25. Retrieved from <http://dx.doi.org/10.1007/s00410-018-1544-4> doi:
 1060 10.1007/s00410-018-1544-4

- 1062 10.1007/s00410-018-1544-4
1063 Wanke, M., Karakas, O., & Bachmann, O. (2019). The genesis of arc dacites:
1064 the case of Mount St. Helens, WA. *Contributions to Mineralogy and*
1065 *Petrology*, 174(1), 1–14. Retrieved from <http://dx.doi.org/10.1007/s00410-018-1542-6> doi: 10.1007/s00410-018-1542-6
1066
1067 Whittington, A. G., Hellwig, B. M., Behrens, H., Joachim, B., Stechern, A., & Vete-
1068 ere, F. (2009). The viscosity of hydrous dacitic liquids: Implications for the
1069 rheology of evolving silicic magmas. *Bulletin of Volcanology*, 71(2), 185–199.
1070 doi: 10.1007/s00445-008-0217-y
1071 Williams, S. D. (2008). CATS: GPS coordinate time series analysis software. *GPS*
1072 *Solutions*, 12(2), 147–153. doi: 10.1007/s10291-007-0086-4
1073 Wong, Y.-Q., & Segall, P. (2019, nov). Numerical Analysis of Time-Dependent
1074 Conduit Magma Flow in Dome-Forming Eruptions With Application to Mount
1075 St. Helens 2004–2008. *Journal of Geophysical Research: Solid Earth*, 124(11),
1076 11251–11273. Retrieved from <https://onlinelibrary.wiley.com/doi/abs/10.1029/2019JB017585> doi: 10.1029/2019JB017585
1077
1078 Wong, Y.-Q., Segall, P., Bradley, A., & Anderson, K. (2017, oct). Constraining
1079 the Magmatic System at Mount St. Helens (2004–2008) Using Bayesian
1080 Inversion With Physics-Based Models Including Gas Escape and Crystalliza-
1081 tion. *Journal of Geophysical Research: Solid Earth*, 122(10), 7789–7812.
1082 Retrieved from <http://doi.wiley.com/10.1002/2017JB014343> doi:
1083 10.1002/2017JB014343
1084 Yang, X.-M., Davis, P. M., & Dieterich, J. H. (1988, may). Deformation from in-
1085 flation of a dipping finite prolate spheroid in an elastic half-space as a model
1086 for volcanic stressing. *Journal of Geophysical Research*, 93(B5), 4249. Re-
1087 trieved from <http://doi.wiley.com/10.1029/JB093iB05p04249> doi:
1088 10.1029/JB093iB05p04249